



# Sparse Bayesian mass-mapping with uncertainties: Full sky observations on the celestial sphere

M. A. Price,<sup>1</sup>★ J. D. McEwen,<sup>1</sup>★ L. Pratley<sup>1,2</sup> and T. D. Kitching<sup>1</sup>

<sup>1</sup>Mullard Space Science Laboratory, University College London, Dorking RH5 6NT, UK

<sup>2</sup>Dunlap Institute for Astronomy and Astrophysics, University of Toronto, ON M5S 3H4, Canada

Accepted 2020 November 10. Received 2020 September 3; in original form 2020 April 20

## ABSTRACT

To date weak gravitational lensing surveys have typically been restricted to small fields of view, such that the flat-sky approximation has been sufficiently satisfied. However, with Stage IV surveys (e.g. *LSST* and *Euclid*) imminent, extending mass-mapping techniques to the sphere is a fundamental necessity. As such, we extend the sparse hierarchical Bayesian mass-mapping formalism presented in previous work to the spherical sky. For the first time, this allows us to construct maximum a posteriori spherical weak lensing dark-matter mass-maps, with principled Bayesian uncertainties, without imposing or assuming Gaussianity. We solve the spherical mass-mapping inverse problem in the analysis setting adopting a sparsity promoting Laplace-type wavelet prior, though this theoretical framework supports all log-concave posteriors. Our spherical mass-mapping formalism facilitates principled statistical interpretation of reconstructions. We apply our framework to convergence reconstruction on high resolution  $N$ -body simulations with pseudo-*Euclid* masking, polluted with a variety of realistic noise levels, and show a significant increase in reconstruction fidelity compared to standard approaches. Furthermore, we perform the largest joint reconstruction to date of the majority of publicly available shear observational data sets (combining DESY1, KiDS450, and CFHTLenS) and find that our formalism recovers a convergence map with significantly enhanced small-scale detail. Within our Bayesian framework we validate, in a statistically rigorous manner, the community’s intuition regarding the need to smooth spherical Kaiser-Squires estimates to provide physically meaningful convergence maps. Such approaches cannot reveal the small-scale physical structures that we recover within our framework.

**Key words:** gravitational lensing; weak – methods: data analysis – methods: statistical – techniques: image processing – large-scale structure of Universe.

## 1 INTRODUCTION

Gravitational lensing is an astrophysical phenomenon through which the geometry of distant galaxies becomes distorted by the intervening matter distribution. Mathematically, this lensing effect is a perturbation by the local matter topology of the null geodesics along which photons travel (Bartelmann & Schneider 2001; Schneider 2005; Grimm & Yoo 2018). As such, gravitational lensing is sensitive to all matter (both visible and invisible) and is thus a natural tool with which to probe the nature of dark matter.

Weak gravitational lensing refers to the vast majority of lensing events for which images are not multiply sourced or ‘strongly lensed’. Equivalently the weak lensing regime can be defined as the regime in which the lensing perturbations remain (to a good approximation) linear. At first order the effect of weak lensing on distant galaxy images manifests itself as two quantities: the spin-0 magnification referred to as the convergence field  $\kappa$ , and a spin-2 perturbation to the ellipticity (third-flattening) referred to as the shearing or shear field  $\gamma$ .

Due to the ‘mass-sheet degeneracy’ there is no way to construct a priori estimates of the intrinsic brightness, hence the convergence

field is an unobservable quantity – theoretically one could infer the convergence field directly from the galaxy sizes, but the intrinsic dispersion is too high (Alsing et al. 2015). However, as the distribution of intrinsic ellipticities has zero mean and sufficiently tight dispersion, averaging sufficient observations within a given pixel can provide an accurate estimator for the shear signal. As such, measurements of the shear field  $\gamma$  are typically taken and inverted to form estimates of  $\kappa$  – coined dark matter mass maps by Clowe et al. (2006).

A large proportion (Taylor, Kitching & McEwen 2018) of cosmological information can be extracted directly from the shear field (Van Waerbeke et al. 2013; Giblin et al. 2018; Fluri et al. 2019), however recently cosmologists have become increasingly interested in extracting information from higher order statistics, such as peak & void statistics and Minkowski functionals, which are typically calculated directly from the convergence field (e.g. Coles & Chiang 2000; Munshi & Coles 2017; Fluri et al. 2018; Peel et al. 2018) – motivating research into optimal mass-mapping techniques. Typically, these higher order statistics aim to probe the non-Gaussian information content of the convergence field.

Mapping from shear to convergence (mass-mapping) requires solving an (often seriously) ill-posed inverse problem – mass-mapping takes the form of a typical noisy deconvolution problem with a spin-2 kernel (Wallis et al. 2017a), which is classically ill-posed. The most naive mass-mapping technique for small fields of

\* E-mail: [m.price.17@ucl.ac.uk](mailto:m.price.17@ucl.ac.uk) (MAP); [jason.mcewen@ucl.ac.uk](mailto:jason.mcewen@ucl.ac.uk) (JCM)

view is planar Kaiser-Squires (KS; Kaiser & Squires 1993) which is direct inversion of the forward model in Fourier space. This estimator does not take into account noise or boundary effects, and so is typically post-processed via convolution with a large Gaussian smoothing kernel, thus heavily degrading the quality of high-resolution non-Gaussian information. Moreover, decomposition of spin-fields on bounded manifolds is known to be degenerate (Bunn et al. 2003) and so for non-trivial masking the KS estimator is ill-defined and can be shown to perform poorly (see Section 5).

Many, perhaps more sophisticated, approaches to mass-mapping on the plane have been developed (e.g. VanderPlas et al. 2011; Jee et al. 2016; Lanusse et al. 2016; Jeffrey et al. 2018) though all either lack a principled statistical framework or rely heavily on assumptions or impositions of Gaussianity. In previous work we present a sparse hierarchical Bayesian formalism for planar mass-mapping (Price et al. 2018, 2019a, b) that provides fully principled statistical uncertainties without the need to assume Gaussianity and without the computational overhead of Markov Chain Monte Carlo (MCMC) methods (e.g. Corless, King & Clowe 2009; Schneider et al. 2015; Alsing et al. 2016).

One key assumption of these ‘planar’ mass-mapping techniques is that the area of interest on the sky can be well approximated as a plane. This assumption is colloquially referred to as the flat-sky approximation. For small-field surveys this approximation is typically justified. However for future wide-field Stage IV surveys mass-mapping must be constructed natively on the sphere (Chang et al. 2018) to avoid errors due to projection effects, which can be large (Wallis et al. 2017a; Vallis, Wallis & Kitching 2018). Naturally one can naively invert the spherical forward model to form the spherical Kaiser-Squires estimator (SKS; Wallis et al. 2017a) which avoids projection effects but is seriously ill-posed, as is the KS method. It should be noted that alternative techniques for spherical reconstruction have also been developed (e.g. Pichon et al. 2010).

In this paper, we extend the previously developed hierarchical Bayesian-sparse formalism to the sphere which, for the first time, allows maximum a posteriori (MAP) convergence reconstruction with principled Bayesian uncertainties in very high-dimensions natively on the sphere without making any assumptions or impositions of Gaussianity. Throughout this paper, we refer to our estimator, formed within this framework, as the DARKMAPPER estimator (and by extension the DARKMAPPER codebase). The reconstruction formalism presented in this paper and any uncertainty quantification techniques that follow support any choice of likelihood or prior such that the posterior function belongs to the (rather comprehensive) set of log-concave functions. As such one can incorporate various experimental or systematic effects in future, e.g. more complex noise models or intrinsic alignment corrections etc.

The structure of this paper is as follows. In Section 2, we provide background mathematical details relevant to the scope of this paper, such as the analysis of spin signals on the sphere, and succinctly review weak gravitational lensing. Following this Section 3 provides a cursory introduction to Bayesian analysis before presenting and discussing both the general hierarchical Bayesian formalism and our DARKMAPPER estimator. In this section, we explicitly outline the likelihood and priors used throughout this paper but place emphasis on the generality of this formalism. Furthermore, we outline how to fold uncertainty in regularization parameters into the hierarchy via the allocation of a suitable (here a conjugate) hyper-prior distribution. In Section 4, we extend previously developed uncertainty quantification techniques to the spherical space and discuss how one should approach constructing custom uncertainty quantification techniques which fit within our formalism. In Section 5, using high

resolution  $N$ -body (Takahashi et al. 2017) simulations, pseudo-Euclid masking (a masking of the galactic plane and the ecliptic) and noise realizations representative of a variety of weak lensing survey eras (including Stage IV), we demonstrate the drastic increase in reconstruction fidelity of DARKMAPPER over SKS. Penultimately, in Section 6 we apply both the SKS and DARKMAPPER estimators to a global weak lensing data set constructed via the concatenation of the majority of publicly available observational data sets. To the best of our knowledge, this is the first such global spherical dark-matter mass-maps. Furthermore, we perform global Bayesian uncertainty quantification on these reconstructions. Finally, in Section 7 we draw conclusions.

## 2 BACKGROUND

Here we present a cursory synopsis of the relevant background required to understand weak lensing on the sphere. In no way is this a complete description and so we recommend the reader follow related papers (McEwen et al. 2015b; Wallis et al. 2017a; Wallis, Wiaux & McEwen 2017b).

### 2.1 Spin- $s$ spherical fields

Local rotations by  $\chi \in [0, 2\pi)$  about the tangent plane centred on the spherical coordinate  $\omega = (\theta, \psi) \in \mathbb{S}^2$  of square integrable spin- $s$  fields for  $s \in \mathbb{Z}$  are defined generally by (Newman & Penrose 1966; Goldberg et al. 1967; McEwen et al. 2013a; Wallis et al. 2017a)

$${}_s f'(\omega) = e^{-is\chi} {}_s f(\omega), \quad (1)$$

where  $\omega = (\theta, \psi)$  are standard spherical coordinates, given by colatitude  $\theta \in [0, \pi)$  and longitude  $\psi \in [0, 2\pi)$ . The natural set of orthogonal basis functions for spherical fields are the spherical harmonics  $Y_{\ell m}(\omega)$ .

When considering spin- $s$  fields on  $\mathbb{S}^2$  the natural set of orthogonal basis functions are the spin-weighted spherical harmonics. The spin-weighted spherical harmonics are generated by application of the spin raising and lowering operators ( $\eth$  and  $\ethbar$ , respectively) to the spherical eigenfunctions  $Y_{\ell m}(\omega)$ . The spin- $s$  raising and lowering operators are given, respectively, by

$$\eth \equiv -\sin^s \theta \left( \frac{\partial}{\partial \theta} + \frac{i \partial}{\sin \theta \partial \psi} \right) \sin^{-s} \theta, \quad (2)$$

$$\ethbar \equiv -\sin^{-s} \theta \left( \frac{\partial}{\partial \theta} - \frac{i \partial}{\sin \theta \partial \psi} \right) \sin^s \theta. \quad (3)$$

On application to  ${}_s Y_{\ell m}(\omega)$  we find the recursion relations,

$$\eth {}_s Y_{\ell m}(\omega) = [(\ell - s)(\ell + s + 1)]^{1/2} {}_{s+1} Y_{\ell m}(\omega), \quad (4)$$

$$\ethbar {}_s Y_{\ell m}(\omega) = -[(\ell + s)(\ell - s + 1)]^{1/2} {}_{s-1} Y_{\ell m}(\omega). \quad (5)$$

Following these recursions, it is clear that any spin- $s$  weighted spherical harmonic can be represented as  $s \in \mathbb{N}$  repeated applications of the spin raising (lowering) operator  $\eth$  to the standard spin-0 spherical harmonic  $Y_{\ell m}$  such that,

$${}_s Y_{\ell m}(\omega) = \left[ \frac{(\ell - s)!}{(\ell + s)!} \right]^{1/2} \eth^s Y_{\ell m}(\omega), \quad (6)$$

for positive semidefinite spin  $0 \leq s \leq \ell$ , and for negative semidefinite spin  $-\ell \leq s \leq 0$  by,

$${}_s Y_{\ell m}(\omega) = (-1)^s \left[ \frac{(\ell + s)!}{(\ell - s)!} \right]^{1/2} \ethbar^{-s} Y_{\ell m}(\omega). \quad (7)$$

The spin- $s$  weighted spherical harmonics form a complete set of orthogonal basis functions which leads to the harmonic representation of a spin- $s$  field  ${}_s f(\omega)$  by

$${}_s f(\omega) = \sum_{\ell=0}^{\infty} \sum_{m=-\ell}^{\ell} {}_s \hat{f}_{\ell m} {}_s Y_{\ell m}(\omega). \quad (8)$$

We can then trivially invert this decomposition to give the spin- $s$  field  ${}_s f(\omega)$  projected on to the spin basis eigenfunctions (i.e. the spin-spherical harmonic coefficients),

$${}_s \hat{f}_{\ell m} = \int_{\mathbb{S}^2} d\Omega(\omega) {}_s f(\omega) {}_s Y_{\ell m}^*(\omega), \quad (9)$$

where the integral is over the sphere  $\mathbb{S}^2$ , and  $d\Omega(\omega) = \sin\theta d\theta d\phi$  is the rotation invariant measure on the sphere. Typically the signal is band-limited at  $\ell_{\max}$  which implies  ${}_s \hat{f}_{\ell m} = 0, \forall \ell \geq \ell_{\max}$  allowing the  $\ell$  summations in equation (8) and the upper limit of the integral in equation (9) to be truncated at  $\ell_{\max}$  to make the computation tractable.

## 2.2 Weak lensing on the sphere

This section provides a basic introduction to weak lensing mass-mapping in the spherical setting. For a more detailed introduction, we refer the reader to popular reviews (e.g. Bartelmann & Schneider 2001; Schneider 2005).

Gravitational lensing is an astrophysical effect which describes the deflection of distant photons as they propagate to us here and now by the intervening local matter distribution. As lensing is sensitive to the local matter distribution (both visible and dark), it provides a natural cosmological probe of dark matter.

Specifically, the weak lensing (WL) regime refers to photons which have angular position on the source plane  $\beta$  (relative to the line-of-sight from observer through the lensing mass) smaller than one Einstein radius  $\theta_E$  to the intervening lensing mass. Mathematically this restricts us to singular solutions of the lens equation,

$$\beta = \theta - \theta_E^2 \frac{\theta}{|\theta|^2}, \quad \text{where} \quad \theta_E = \sqrt{\frac{4GM}{c^2} \frac{f_K(r-r')}{f_K(r)f_K(r')}}, \quad (10)$$

for angular diameter distance  $f_K$ , defined in the usual sense, which is dependent on the curvature of the Universe  $K$ . The Universe has been observed to be essentially flat (Planck Collaboration VI 2020) and so to a good approximate  $K \approx 0 \Rightarrow f_K(r) \approx r$ , where  $r$  is the comoving distance.

Galaxies are naturally sparsely distributed across the sky and so the overwhelming majority of observations fall within the weak lensing regime (Bartelmann & Schneider 2001). Now consider a lensing potential  $\phi$  which is the weighted integral along the line of sight of the local Newtonian potential  $\Phi$ ,

$$\phi(r, \omega) = \frac{2}{c^2} \int_0^r dr' \frac{f_K(r-r')}{f_K(r)f_K(r')} \Phi(r', \omega). \quad (11)$$

Poisson's equation must then be satisfied by the local Newtonian potential,

$$\nabla^2 \Phi(r, \omega) = \frac{3\Omega_M H_0^2}{2a(r)} \delta(r, \omega), \quad (12)$$

where  $\delta(r, \omega)$  is the fractional overdensity,  $H_0$  is the Hubble constant,  $a(r)$  is the scale-parameter, and  $\Omega_M$  is the matter density parameter. At first order two physical lensing quantities can be constructed, these being the gravitational shear  ${}_2\gamma$  and the convergence  ${}_0\kappa$  (Bartelmann & Schneider 2001; Schneider 2005), where the subscripts reflect the spin of each field.

These quantities are related to the underlying scalar integrated potential  ${}_0\phi$  by the relations (Castro, Heavens & Kitching 2005; Wallis et al. 2017a),

$${}_0\kappa(r, \omega) = \frac{1}{4} (\bar{\partial}\bar{\partial} + \bar{\partial}\bar{\partial}) {}_0\phi(r, \omega), \quad (13)$$

$${}_2\gamma(r, \omega) = \frac{1}{2} \bar{\partial}\bar{\partial} {}_0\phi(r, \omega), \quad (14)$$

If we now project these values into their harmonic representations by equation (9) we find the harmonic space relations,

$${}_0\hat{\kappa}_{\ell m} = -\frac{1}{2} \ell(\ell+1) {}_0\hat{\phi}_{\ell m}, \quad (15)$$

$${}_2\hat{\gamma}_{\ell m} = \frac{1}{2} \sqrt{\frac{(\ell+2)!}{(\ell-2)!}} {}_0\hat{\phi}_{\ell m}. \quad (16)$$

We can then trivially draw a relationship between  ${}_2\hat{\gamma}_{\ell m}$  and  ${}_0\hat{\kappa}_{\ell m}$  in harmonic space,

$${}_2\hat{\gamma}_{\ell m} = \mathcal{W}_{\ell} {}_0\hat{\kappa}_{\ell m}, \quad (17)$$

which is the spherical forward model. We have defined a mapping kernel (as in e.g. Wallis et al. 2017a) in harmonic space such that,

$$\mathcal{W}_{\ell} = \frac{-1}{\ell(\ell+1)} \sqrt{\frac{(\ell+2)!}{(\ell-2)!}}. \quad (18)$$

This mapping is analogous to the planar forward model (Price et al. 2018) but now defined on  $\mathbb{S}^2$ . This mapping can trivially be inverted to define the so-called ‘Spherical Kaiser-Squires’ (SKS; Wallis et al. 2017a) convergence estimator,

$${}_0\hat{\kappa}_{\ell m}^{\text{SKS}} = \mathcal{W}_{\ell}^{-1} {}_2\hat{\gamma}_{\ell m}^{\text{obs}}, \quad (19)$$

where superscript ‘obs’ refers to the observations (or measurements) of a given shear field  ${}_2\gamma$ . A real-space representation of this mapping exists (Wallis et al. 2017a).

It is of interest to notice certain similarities between the SKS estimator  ${}_0\kappa_{\text{SKS}}$  and the maximum-likelihood estimator (MLE) denoted  ${}_0\kappa_{\text{MLE}}$ , which is defined by maximization of the likelihood (i.e. an implicit assumption of a flat prior on  $\kappa$ ). Suppose the noise properties are assumed to be Gaussian (as is common), then the likelihood is given by

$$P(\gamma|\kappa) \propto |\Sigma|^{-1/2} \exp^{-\frac{1}{2}\chi^2}, \quad (20)$$

for  $\chi^2 \equiv (\gamma - \Phi\kappa)^T \Sigma^{-1} (\gamma - \Phi\kappa)$  where  $\Phi$  is simply the forward model and  $\Sigma$  is the noise covariance. The solution which minimizes the likelihood is thus given by

$${}_0\kappa_{\text{MLE}} = (\Phi^T \Sigma^{-1} \Phi)^{-1} \Phi^T \Sigma^{-1} \gamma. \quad (21)$$

Therefore for the idealized SKS estimator  $\Phi^{-1}\gamma$  to be equivalent to the MLE estimator we require  $\Phi^{-1}$  and  $(\Phi^T \Sigma^{-1} \Phi)^{-1} \Phi^T \Sigma^{-1}$  to be equivalent operators. Provided  $\Phi$  is invertible the  $\Sigma$  terms above trivially cancel resulting in the remaining terms  $(\Phi^T \Phi)^{-1} \Phi^T$ , which reduce to the idealized SKS estimator – note that in the idealized setting  $\Phi$  is straightforwardly invertible given both the spherical harmonic transform and equation (18) are invertible (ignoring the monopole  $\ell = 0$ ). Thus in this setting the idealized SKS and MLE estimator are equivalent.

However, in practical applications the forward model (e.g. with PSF corrections, complex masking, etc.) is unlikely to be invertible and hence the SKS and MLE estimators differ in practice. Furthermore, due to limited observation quality (discussed in Section 5.2.1) the noise covariance is typically large in magnitude. In such settings

the inverse problem is strongly ill-posed and thus significant regularization (introduced through the prior term) is required to stabilize the inversion. As such, a flat prior MLE results in unregularized solutions which are highly unlikely to perform well (noise present in  $\gamma$  is very likely to propagate directly into the  $\kappa$  estimate). This noise propagation is well-known, hence the SKS estimator used in practice always includes a smoothing post-processing step (convolution with an arbitrary smoothing kernel) in an attempt to mitigate this noise. Consequently, the SKS estimator used in practice does not support a principled statistical interpretation.

### 3 SPHERICAL BAYESIAN MASS-MAPPING

Hierarchical Bayesian frameworks facilitate a natural, mathematically principled approach to uncertainty quantification. For an elegant and approachable introduction to Bayesian methods see Trotta (2017). This section introduces Bayesian inference and proceeds to demonstrate how one may cast the spherical mass-mapping inversion as a hierarchical Bayesian inference problem. For notational ease, we drop spin subscripts on  $\kappa$  and  $\gamma$  henceforth.

#### 3.1 Bayesian inference

First consider the posterior distribution given by Bayes' Theorem,

$$p(\kappa|\gamma; \mathcal{M}) = \frac{p(\gamma|\kappa; \mathcal{M})p(\kappa; \mathcal{M})}{\int_{\mathbb{C}^N} p(\gamma|\kappa; \mathcal{M})p(\kappa; \mathcal{M})d\kappa}, \quad (22)$$

where the likelihood function  $p(\gamma|\kappa; \mathcal{M})$  represents the probability of observing a shear field  $\gamma$  given a convergence field  $\kappa$  and some well defined model  $\mathcal{M}$  (which includes both the mapping  $\Phi : \kappa \mapsto \gamma$  and some assumptions of the noise model). The second term in the numerator,  $p(\kappa; \mathcal{M})$  is referred to as the prior which encodes some a priori knowledge as to the nature of  $\kappa$ . Finally, the integral denominator is the Bayesian evidence (or marginal likelihood) which can be used for model comparison, though we do not consider this within the scope of this paper.

One approach to estimate the convergence field is given by maximizing the posterior odds conditional on the measurements  $\gamma$  and model  $\mathcal{M}$ . Such a solution is referred to as the maximum a posteriori (MAP) solution,  $\kappa^{\text{map}}$ . This can be done by either maximization of the posterior or – due to the monotonicity of the logarithm function – minimization of the log-posterior,

$$\underset{\kappa}{\operatorname{argmax}} \{p(\kappa|\gamma; \mathcal{M})\} \equiv \underset{\kappa}{\operatorname{argmin}} \{-\log(p(\kappa|\gamma; \mathcal{M}))\}. \quad (23)$$

This is a particularly helpful realization as the latter problem is more straightforward to compute and, for log-concave posteriors, allows one to pose the problem as a convex optimization problem for which one may draw on the field of convex optimization.

#### 3.2 Spherical sparse mass-mapping

In this paper, we consider the ill-posed linear inverse problem of recovering the complex discretized spherical convergence  $\kappa \in \mathbb{C}^{N_{S^2}}$  on the complex  $S^2$ -sphere from a typically incomplete ( $M < N$ ) set of  $M$  complex discretized shear measurements  $\gamma \in \mathbb{C}^M$ . Throughout we adopt the McEwen-Wiaux (MW) pixellization scheme, which provides theoretically exact spin spherical harmonic transforms (SSHT) due to exact quadrature (McEwen & Wiaux 2011).

We begin by defining the measurement operator (operator which encodes the forward model) which maps from a fiducial convergence

field to the observed shear measurements

$$\Phi \in \mathbb{C}^{M \times N_{S^2}} : \kappa \in \mathbb{C}^{N_{S^2}} \mapsto \gamma \in \mathbb{C}^M. \quad (24)$$

In the spherical setting, by noting the spherical lensing forward model given by equation (18) this measurement operator naturally takes the form,

$$\Phi = M_2 \tilde{Y} W {}_0Y, \quad (25)$$

where  ${}_sY$  and  ${}_s\tilde{Y}$  represent the forward and inverse spin- $s$  spherical harmonic transforms, respectively,  $M$  is a masking operator, and  $W$  is harmonic space multiplication by the kernel  $\mathcal{W}_\ell$  defined in equation (18). The adjoint-measurement operator can then be shown to be,

$$\Phi^\dagger = {}_0Y^\dagger W {}_2\tilde{Y}^\dagger M^\dagger, \quad (26)$$

where it should be noted that from symmetry  $W$  is trivially self-adjoint. Additionally, it is important to note that adjoint ( $\dagger$ ) spin- $s$  spherical harmonic transforms are not equivalent to the corresponding inverse spherical harmonic transforms – an important caveat often overlooked throughout the field.

##### 3.2.1 Likelihood function

Suppose now that measurements  $\gamma$  are acquired under some additive Gaussian noise  $n_i \sim \mathcal{N}(0, \sigma_i^2) \in \mathbb{C}^M$  where  $\sigma_i$  is the noise standard deviation of a given pixel which is primarily dependent on the number of observations within said pixel, which is in turn dependent on the pixel size and number density of galaxy observations. Then the data acquisition model is simply given by

$$\gamma = \Phi\kappa + n. \quad (27)$$

In such a setting the Bayesian likelihood function (data fidelity term) is given by the product of Gaussian likelihoods defined on each pixel with pixel noise variance  $\sigma_i^2$ , which is to say an overall multivariate Gaussian likelihood of known covariance  $\Sigma = \operatorname{diag}(\sigma_1, \sigma_2, \dots, \sigma_M) \in \mathbb{R}^{M \times M}$ . Let  $\Phi_{i\kappa}$  be the value of  $\Phi\kappa$  at pixel  $i$ , then the overall likelihood is then defined as,

$$\begin{aligned} p(\gamma|\kappa) &\propto \prod_{i=0}^M \exp\left(\frac{-(\Phi_{i\kappa} - \gamma_i)^2}{2\sigma_i^2}\right) = \prod_{i=0}^M \exp\left(\frac{-1}{2}(\bar{\Phi}_{i\kappa} - \bar{\gamma}_i)^2\right), \\ &= p(\gamma|\kappa) \propto \exp\left(\frac{-\|\bar{\Phi}\kappa - \bar{\gamma}\|_2^2}{2}\right), \end{aligned} \quad (28)$$

where  $\|\cdot\|_2$  is the  $\ell_2$ -norm and  $\bar{\Phi} = \Sigma^{-\frac{1}{2}}\Phi$  is a composition of the measurement operator and an inverse covariance weighting as defined in Section 3.2. Effectively this covariance weighting leads to measurements  $\bar{\gamma} = \Sigma^{-\frac{1}{2}}\gamma$  which whiten the typically non-uniform noise variance in the observational data (shear field).

This likelihood is therefore structured to correctly account for the covariance of observational data. In this case, the covariance matrix is taken to be diagonal but not necessarily proportional to the identity matrix – therefore accounting for varied numbers of observations per pixel. There are several points which should be noted. In the above we have explicitly ignored the complicating factor of intrinsic galaxy alignments which in practice would lead to non-diagonal covariance. This extension can easily be supported, given a sound understanding of the effects of intrinsic alignments on the data covariance (which in practice may be challenging).

Additionally here we, for simplicity, assume each pixel contains a sufficient number of galaxy observations that a central limit theorem (CLT) argument for pixel noise can be justified. Largely

this assumption is acceptable, however as the resolution increases (pixel size decreases) the noise becomes increasingly non-Gaussian.

Finally, the forward model considered here (Section 3.2) begins from  $\kappa$  and ends at masked, gridded  $\gamma$  measurements, however there are several steps which must take place before one acquires such measurements. One may therefore wish to extend this model to incorporate such complicating factors as pixelization effects, reduced shear (see Section 3.3.1), point squared function (PSF) errors etc.

It should then be explicitly noted that this mass-mapping formalism requires only that the posterior belong to the (rather comprehensive) set of log-concave functions, and as such one can directly interchange the noise model or introduce complicating factors where desired provided the posterior remains log-concave.

### 3.2.2 Prior function

As this inverse problem is ill-posed (often seriously), MLEs are suboptimal and must be regularized by some prior assumption as to the nature of the convergence field. In this work we select a sparsity promoting, Laplace-type prior in the form of the  $\ell_1$ -norm  $\|\cdot\|_1$  – though as discussed in Section 3.2.1 this formalism supports any log-concave priors of which there are many to choose from (e.g. most exponential family priors).

Laplace-type priors are often adopted when one wishes to promote sparsity in a given dictionary or basis. Wavelets  $\Psi$  are localized in both the frequency and spatial domains and thus constitute a naturally sparsifying dictionary for most physical signals. There are several wavelet constructions on the sphere that may be considered (see e.g. Schröder & Sweldens 1995; Barreiro et al. 2000; Narcowich, Petrushev & Ward 2006; Starck et al. 2006; Marinucci et al. 2007; McEwen & Scaife 2008; Wiaux et al. 2008; Baldi et al. 2009; McEwen, Wiaux & Eyers 2011; Chan et al. 2017; McEwen, Durastanti & Wiaux 2018; McEwen & Price 2019) with varying localization and uncorrelation properties. In this paper we adopt the scale-discretized wavelets (Wiaux et al. 2008; Leistedt et al. 2013; McEwen, Vanderghaynst & Wiaux 2013b; McEwen et al. 2015a) scheme as not only does it satisfy quasi-exponential localization and asymptotic uncorrelation properties (McEwen et al. 2018) but also supports directionality which may often be of interest for the weak lensing setting.

We specifically adopt a Laplace-type wavelet log-prior  $\|\Psi(\cdot)\|_1$ . Note that as  $\|\cdot\|_1$  is a discretization of the continuous  $\ell_1$ -norm it must be reweighted by wavelet pixel size, which in practice is as simple as multiplying a given wavelet coefficient by a factor proportional to  $\sin(\theta)$  where  $\theta$  is the angular deviation of the given pixel from the pole. Throughout this paper any reference to the  $\ell_1$ -norm applied to a spherical space refers explicitly to this spherically reweighted norm.

With our choice of  $\ell_1$ -norm regularization the prior can be written compactly as

$$p(\kappa) \propto \exp\left(-\mu \|\Psi^\dagger \kappa\|_1\right), \quad (29)$$

where  $\Psi^\dagger$  is the analysis forward-adjoint spherical wavelet transforms (see equation A8 in the appendix) with coefficients  $\Psi_i^\dagger$ , and  $\mu \in \mathbb{R}^+$  is the regularization parameter. It is assumed here that the spherical wavelet dictionary  $\Psi$  is a naturally sparsifying dictionary for the convergence field defined on the sphere. In practice one may select whichever dictionary one's prior knowledge of the convergence indicates is likely to be highly sparsifying.

Conceptually, a sparsity-promoting prior can be thought of as a mathematical manifestation of *Occam's Razor* – the philosophical notion that the simplest answer is usually the best answer. Mathematically, this is equivalent to down-weighting solutions with large numbers of non-zero coefficients, which may match the noisy data perfectly, in favour of a less perfect match but with significantly fewer non-zero coefficients.

Alternatively, one may view sparsity priors (in this context) as a relative assumption of the sparsity of the true signal and noise signal when projected into a sparsifying dictionary. This is to say that the assumption is that the noise signal will be less sparse in  $\Psi$  than the true signal. Typically noise signals are relatively uniformly distributed in wavelet space, whereas most physical signals are sparsely distributed and therefore this relative interpretation of the sparsity prior makes reasonable sense (Mallat 1999).

Note that the only constraint on the posterior is that it must be log-concave (such that the log-posterior is convex). Hence one can select any log-concave prior within this framework, e.g. one could select an  $\ell_2$ -norm prior which with minor adjustments produces Wiener filtering (see Horowitz, Seljak & Aslanyan 2018, for alternate iterative Wiener filtering approaches), or a flat prior which produces the maximum-likelihood estimate (MLE).

### 3.3 Implementation

The minimization of the log-posterior in equation (23) is (in the analysis setting) therefore precisely the same as solving,

$$\kappa^{\text{map}} = \underset{\kappa}{\operatorname{argmin}} \left\{ \underbrace{\mu \|\Psi^\dagger \kappa\|_1 + \frac{\|\bar{\Phi}\kappa - \bar{\gamma}\|_2^2}{2}}_{\text{Objective function}} \right\}. \quad (30)$$

The bracketed term on the RHS is referred to as the objective function. We solve this convex optimization problem using the S2INV (Price et al., in preparation) code which is largely built around the SOPT C++ object oriented framework<sup>1</sup> (Carrillo, McEwen & Wiaux 2012; Carrillo et al. 2013; Onose et al. 2016; Pratley et al. 2018), utilizing an adapted proximal forward–backward splitting algorithm (Combettes & Pesquet 2009), although a variety of alternate algorithms are provided within S2INV (Price et al., in preparation). Wavelet transforms on the sphere are computed using S2LET<sup>2</sup> (McEwen & Wiaux 2011; Leistedt et al. 2013; McEwen et al. 2015a, b; Chan et al. 2017; McEwen et al. 2018), which in turn makes use of SSHT<sup>3</sup> (McEwen & Wiaux 2011; McEwen et al. 2013a) to compute spherical harmonic transforms and SO3<sup>4</sup> (McEwen et al. 2015a) to compute Wigner transforms.

To deal with the non-differentiable  $\ell_1$ -norm prior, gradient operators  $\nabla$  are in some sense replaced by proximal operators when applied to the non-differentiable term (Moreau 1962). The iteration steps are provided in the schematic of Fig. 1, for full details of the derivation of the proximal forward–backward algorithm iterations look to Combettes & Pesquet (2009). These primary optimizations are terminated once the objective function is updated by less than a set threshold (in our experiments  $10^{-6}$ ) between iterations.

<sup>1</sup><https://github.com/astro-informatics/sopt>

<sup>2</sup><http://astro-informatics.github.io/s2let/>

<sup>3</sup><https://astro-informatics.github.io/ssht/>

<sup>4</sup><http://astro-informatics.github.io/so3/>

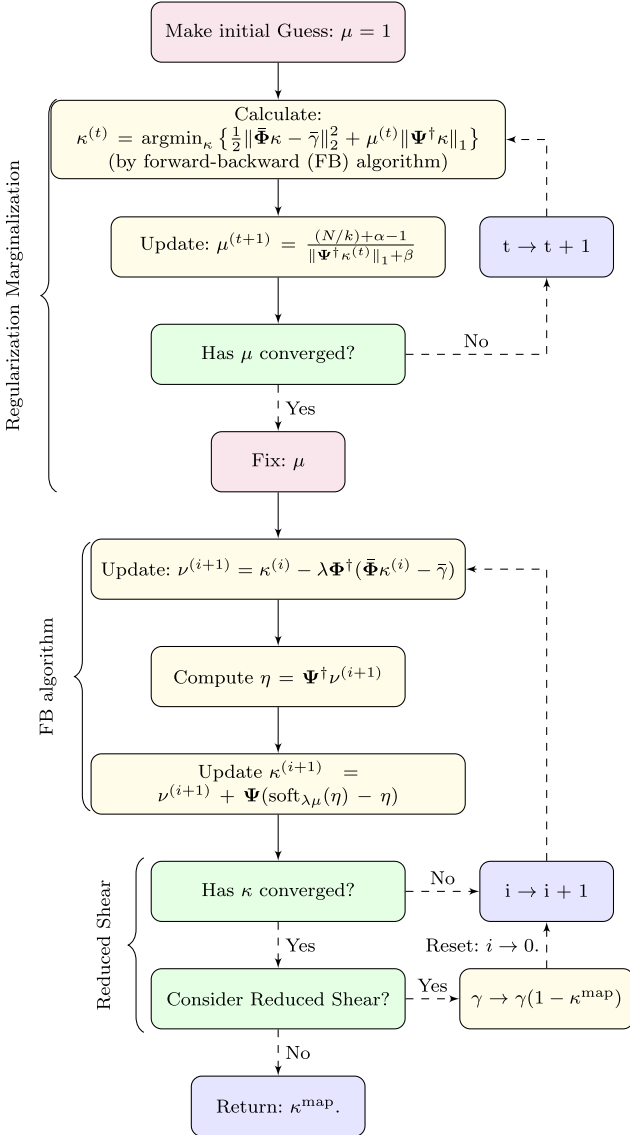


**Figure 1.** Schematic of proximal forward–backward splitting algorithm used (Combettes & Pesquet 2009). Note that the first iterative block represents the Majorize–Minimization (MM) algorithm marginalization over the regularization parameter (which here is treated as a nuisance parameter), the second iterative block represents the primary proximal forward–backward iterations, and the final (optional) block represents the reduced shear outer iterations. Note that the  $\text{soft}_{\lambda, \mu}(\eta)$  operation is the soft thresholding operation, which is the proximal projection of the  $\ell_1$ -norm (see e.g. Pereyra 2017; Cai, Pereyra & McEwen 2018a, b, for details).

### 3.3.1 Reduced shear

Fig. 1 displays a schematic representation of the steps taken in computing  $\kappa^{\text{map}}$ . A degeneracy between the convergence field  $\kappa$  and shear field  $\gamma$  exists, and as such  $\gamma$  is not a true observable. Instead the reduced shear  $g$  is the true observable where,

$$g(\omega) = \frac{\gamma(\omega)}{1 - \kappa(\omega)}. \quad (31)$$

When working sufficiently within the weak lensing regime  $\kappa \ll 1$  and  $\gamma \approx g \ll 1$ . Although typically the reduced shear need not be accounted for, for completeness we correct for the reduced shear (Mediavilla et al. 2016; Wallis et al. 2017a; Price et al. 2018). We add

correcting iterations outside our primary iterations to maintain the linearity of the overall reconstruction. Our reduced shear correction iterations are displayed schematically in the final loop of Fig. 1.

Reduced shear iterations are deemed to have converged once the convergence update  $\max_j |\kappa_j^{(i)} - \kappa_j^{(i+1)}| < 10^{-10}$  where  $j$  runs over all pixels (as in Wallis et al. 2017a).

### 3.3.2 Bayesian regularization parameter

For recovered statistics to be truly principled, the regularization parameter must necessarily be folded into the hierarchy or correctly marginalized over. One way to do this was recently developed (Pereyra, Bioucas-Dias & Figueiredo 2015) and shown to work well in the planar weak lensing setting (Price et al. 2018).

This Bayesian hierarchical inference approach assumes a gamma distribution hyper-prior

$$p(\mu) = \frac{\beta^\alpha}{\Gamma(\alpha)} \mu^{\alpha-1} e^{-\beta\mu} \mathbb{1}_{\mathbb{R}^+}(\mu), \quad (32)$$

with weakly dependent hyperparameters  $\alpha$  and  $\beta$  which without loss of generality can be fixed at  $\alpha = \beta = 1$ . We then iterate (Pereyra et al. 2015) to effectively marginalize over  $\mu$  which is treated as a nuisance parameter in the main body of our hierarchy. These iterations are,

$$\kappa^{(t)} = \arg\min_{\kappa} \left\{ \frac{1}{2} \|\bar{\Phi}\kappa - \bar{\gamma}\|_2^2 + \mu^{(t)} \|\Psi^\dagger \kappa\|_1 \right\}, \quad (33)$$

$$\mu^{(t+1)} = \frac{(N/k) + \alpha - 1}{\|\Psi^\dagger \kappa^{(t)}\|_1 + \beta}, \quad (34)$$

where the log-prior  $\|\Psi^\dagger \kappa\|_1$  is  $k$ -homogeneous. Note that a sufficient statistic (log-prior) is  $k$ -homogeneous if  $\exists k \in \mathbb{R}^+$  such that,

$$f(\eta x) = \eta^k f(x), \quad \forall x \in \mathbb{R}^M, \quad \forall \eta > 0. \quad (35)$$

Further note that all norms, composite norms, and compositions of norms with linear operators are 1-homogeneous, i.e.  $k = 1$ . See Pereyra et al. (2015) for further details. These regularization–marginalization iterations are terminated when the update to the regularization parameter is less than 1 per cent i.e.  $|\mu^{(i+1)} - \mu^{(i)}|/\mu^{(i)} < 0.01$ .

### 3.3.3 Computational efficiency

As discussed in 3.3 all iterations consist of a forward step which includes application of the measurement operator before computing the data fidelity term, followed by the backward step which includes application of the spherical wavelet transform.

The measurement operator is dominated by the spin spherical harmonic transforms which scale as  $\mathcal{O}(L^3)$ . Similarly the computational efficiency of the wavelet transform is dominated by underlying harmonic transforms, however with directionality  $N$  (i.e. wavelet on the rotation group) the transform scales as  $\mathcal{O}(N \times L^3)$ . The overall forward–backward algorithm scales additively as  $\mathcal{O}(K \times (N + 1) \times L^3) \sim \mathcal{O}(K \times N \times L^3)$ , where  $K$  is the total number of iterations required for convergence.

The SKS operator also requires the application of spin spherical harmonic transforms and therefore scales as  $\mathcal{O}(L^3)$ . However the SKS method requires only a single application of the transform and thus the ratio of computational efficiency between the two algorithms effectively scales as  $\mathcal{O}(K \times N)$  – which is to say the difference in computational efficiency is primarily determined by the choice of wavelet complexity and the magnitudes of the associated convergence criteria.

In practice, including the marginalization preliminary iterations and subsequent annealing iterations to optimize convergence, we find  $\mathcal{O}(10^2)$  iterations are sufficient for convergence. We consider axisymmetric wavelets ( $N = 1$ ) in this article, thus the DARKMAPPER algorithm is  $\mathcal{O}(10^2)$  times slower than SKS but with greatly superior reconstruction performance and the ability to quantify uncertainties in a statistically principled manner.

It is interesting to note that MCMC methods typically require a very large number of samples, with each individual sample requiring at least one spin spherical harmonic transform. Therefore the increase in computational efficiency of this approximate Bayesian inference over sampling methods is roughly given by  $\mathcal{O}(n_{\text{samples}}/10^2)$ , where  $n_{\text{samples}}$  is the total number of samples required for convergence of a given MCMC sampling method. As MCMC methods often require at least  $\mathcal{O}(10^6)$  this increase in computation speed is (many) orders of magnitude. In the spherical setting an  $\mathcal{O}(10^4)$  increase in computation speed results in computations which would take  $\mathcal{O}(\text{decades})$  taking  $\mathcal{O}(\text{days})$ .

#### 4 BAYESIAN UNCERTAINTY QUANTIFICATION

Though MAP estimates provide high-fidelity estimates of the convergence field, uncertainties on these estimates are a necessity if one aims to make statistically principled inferences. Generally, for scientific inference one should prioritize principled uncertainties over image aesthetics.

Bayesian inference approaches as presented in Section 3 provide principled statistical frameworks through which quantification of uncertainty on recovered statistics comes naturally from the posterior. Typically the posterior cannot be evaluated analytically, and so MCMC sampling methods must be used. In moderate to low dimensional settings for computationally cheap functions, MCMC chains can feasibly be computed. However, in high dimensional spherical settings, MCMC techniques quickly become challenging to compute.

Bespoke MCMC techniques have been developed for the weak lensing setting (e.g. Corless et al. 2009; Schneider et al. 2015; Alsing et al. 2016) which can improve computational efficiency, yet these methods will find it challenging to accommodate future ‘Big Data’ from high-resolution wide-field surveys. Furthermore, these sometimes come with additional restrictions (e.g. some are restricted to Gaussian priors). This provides strong motivation for the development of fast, approximate Bayesian inference approaches (Pereyra 2017; Cai et al. 2018b; Price et al. 2018, 2019a, b), the uncertainty quantification of which we extend to the complex  $\mathbb{S}^2$ -sphere and present in this section.

##### 4.1 Highest posterior density region

At  $100(1 - \alpha)$  per cent confidence a subset  $C_\alpha \in \mathbb{C}^{N_{\mathbb{S}^2}}$  of the posterior space is considered a credible region of the posterior *if and only if* the integral equation,

$$p(\kappa \in C_\alpha | \gamma) = \int_{\kappa \in \mathbb{C}^{N_{\mathbb{S}^2}}} p(\kappa | \gamma) \mathbb{1}_{C_\alpha} d\kappa = 1 - \alpha, \quad (36)$$

is satisfied, where we have used the set indicator function  $\mathbb{1}_{C_\alpha}$ , defined to be,

$$\mathbb{1}_{C_\alpha} = \begin{cases} 1 & \text{if, } \kappa \in C_\alpha \\ 0 & \text{if, } \kappa \notin C_\alpha. \end{cases} \quad (37)$$

Theoretically there are infinitely many regions which satisfy the integral in equation (36). However, the decision-theoretic optimal

region – in the sense of minimum volume – is the Highest Posterior Density (HPD) credible-region, which is given by (Robert 2001)

$$C_\alpha := \{\kappa : f(\kappa) + g(\kappa) \leq \epsilon_\alpha\}, \quad (38)$$

where the combination  $f(\kappa) + g(\kappa)$  is our objective function derived in Section 3.3, and  $\epsilon_\alpha$  is an isocontour (i.e. level-set) of the log-posterior.

However, in high dimensional ( $N \gg 1$ ) settings  $\epsilon_\alpha$  (and therefore  $C_\alpha$ ) becomes particularly difficult to compute, thus motivating the development of alternate approaches that are fast and approximate. Recent advances in probability concentration theory have led to the derivation (Pereyra 2017) of a conservative approximate credible-region  $C'_\alpha$  for log-concave distributions. This approximate region is defined as,

$$C'_\alpha := \{\kappa : f(\kappa) + g(\kappa) \leq \epsilon'_\alpha\}, \quad (39)$$

such that,

$$\epsilon'_\alpha = f(\kappa^{\text{map}}) + g(\kappa^{\text{map}}) + \tau_\alpha \sqrt{N} + N, \quad (40)$$

is the approximate level-set threshold with constant  $\tau_\alpha = \sqrt{16 \log(3/\alpha)}$ . Recall that  $N$  is the dimension of  $\kappa \in \mathbb{C}^{N_{\mathbb{S}^2}}$  which for equiangular spherical sampling (MW; McEwen & Wiaux 2011) is given by,

$$N_{\text{MW}} \equiv \ell_{\text{max}}(2\ell_{\text{max}} - 1) \approx 2\ell_{\text{max}}^2, \quad (41)$$

for signals with angular band-limit  $\ell_{\text{max}}$ . An upper bound on the error introduced through this approximation has been shown to exist (Pereyra 2017) and is given by,

$$0 \leq \epsilon'_\alpha - \epsilon_\alpha \leq \eta_\alpha \sqrt{N} + N, \quad (42)$$

where  $\eta_\alpha = \sqrt{16 \log(3/\alpha)} + \sqrt{1/\alpha}$ . This error scales at most linearly with  $N$  and in high dimensional settings can be somewhat large, though in practice we find this error upper-bound to be extremely conservative (Price et al. 2019b).

Note that the error is positive semidefinite which corroborates the assertion that  $C'_\alpha$  is a conservative approximation. Mathematically, this is to say that the true HPD credible region  $C_\alpha$  is subset of the approximate HPD credible region  $C'_\alpha$  i.e.  $C_\alpha \subseteq C'_\alpha$ . This ensures that if some convergence field  $\kappa \notin C'_\alpha$  then necessarily  $\kappa \notin C_\alpha$ .

Further note that although we adopt the approximate level-set threshold derived in Pereyra (2017) in this work, research into these types of bounds is a relatively new area of study. Thus, if and when new (more constraining) bounds are derived they can trivially be substituted here.

##### 4.2 General application

Having introduced the concept of an approximate HPD-credible region  $C'_\alpha$  of the posterior, the question then immediately arises as to how one can utilize this information in practice. In MCMC sampling type approaches, one may simply use the recovered samples to quantify uncertainty at well defined confidence on specific properties of the recovered posterior. In our setting, we have recovered only the MAP solution in a form which supports trivial computation of the approximate level-set threshold, and thus  $C'_\alpha$ .

With such limited posterior knowledge one may only ask whether a surrogate solution (an adjusted convergence map) does or does not belong to  $C'_\alpha$ . In effect this is to say that in our formalism all questions of the posterior must be cast as Bayesian hypothesis tests of varying complexity (Price et al. 2018, 2019a). Some examples are provided in the following subsections.

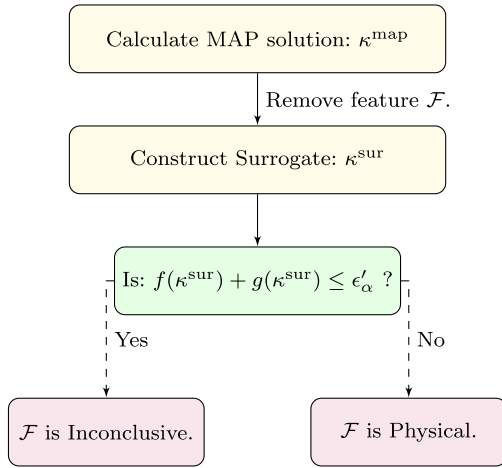


**Figure 2.** Schematic of hypothesis testing (Price et al. 2018). The feature  $\mathcal{F}$  is entirely general and can be constructed by any well defined operator on the MAP solution  $\kappa^{\text{map}}$ .

#### 4.2.1 Bayesian hypothesis testing

A Bayesian hypothesis test on the posterior (see Fig. 2) is simply: the MAP convergence is recovered, a feature of that map is removed<sup>5</sup> to form a surrogate map  $\kappa^{\text{sur}}$ , if  $\kappa^{\text{sur}} \notin C'_\alpha$ , then  $\kappa^{\text{sur}} \notin C_\alpha$ , and thus the hypothesis that feature of interest is insignificant is rejected at some well defined confidence, implying that the feature cannot be deemed insignificant at said confidence (for more details look to Cai et al. 2018b; Price et al. 2018).

One can envisage constructing substantially more complicated uncertainty quantification techniques via iterative application of Bayesian hypothesis testing or by more complicated individual Bayesian hypothesis tests.

#### 4.2.2 Local credible intervals

The next most straightforward uncertainty quantification technique is given by the notion of local credible intervals (Cai et al. 2018b; Price et al. 2019b) which are in effect pixel-level Bayesian uncertainty (error) bars on recovered maps. Conceptually these are formed by splitting the recovered MAP estimate into superpixels (groups of adjacent pixels), then within each superpixel (keeping all other pixels fixed at their MAP values) iteratively increasing (decreasing) the recovered pixel intensity and thus constructing surrogate solutions, checking whether these surrogate solutions belong to  $C'_\alpha$ . Once the maximum (minimum) superpixel intensity is located (typically via bisection) the difference (maximum–minimum) is taken to be the range of values which cannot be rejected for a recovered superpixels intensity – hence the notion of these representing pixel level Bayesian uncertainty (error) bars.

#### 4.2.3 Uncertainty quantification of global features

For science, in particularly for cosmology, it is often perhaps more informative to leverage the concept of Bayesian hypothesis testing to consider global structure, and therefore consider global (or aggregate) statistics of a recovered field. To do so one must simply define a logically consistent algorithm which constructs surrogate

convergence solutions that are representative of the global question they wish to ask of the recovered convergence field, after which the process follows in much the same way as demonstrated for forming local credible intervals.

It should, however, be noted that one must be careful how one poses these global questions, as the questions of interest are often inherently non-convex and must be solved via decision theory methods. A good example of how one can apply hypothesis testing to global structure can be found in Price et al. (2019a) where the Bayesian uncertainty in the aggregate peak statistic is recovered.

Here we have discussed only a few possible uncertainty quantification techniques which are supported by this formalism, though in practice following the methodology outlined above one can form uncertainty quantification techniques around a far more comprehensive set of global features (or equally statistics) provided a few important caveats are understood: the process of Bayesian hypothesis tests suggested to quantify a specified uncertainty are well defined and clearly explained, the limitations of any method are fully acknowledged, and the results are interpreted correctly so as to mitigate unjustified statistical statements. We present a specific example on current cosmic shear data in Section 6.

#### 4.2.4 The curse of dimensionality

Finally, it is academic to note that the concept of changing only a small number of pixels of a given map whilst fixing the remaining at their MAP values is explicitly recovering conditional probabilities which are by definition the largest possible uncertainties. Though this is precisely what one requires of such approximations it highlights an inherent drawback of such approaches. As the approximate level-set threshold scales with the total dimension of the inference in high dimensional cases, the uncertainty of any individual local structure within an image becomes large.

Conceptually this makes sense as the higher the dimensionality of the problem, the more statistical fluctuations occur and thus the higher the chance that a statistical fluctuation produced the feature of interest. As such, for anything higher than moderate dimensional settings local uncertainties become very large and one should prioritize global or aggregate statistics.

## 5 SIMULATIONS

In this section, we apply the spherical Kaiser–Squires (SKS) estimator, both with and without post-processing smoothing, and the spherical sparse hierarchical Bayesian (DARKMAPPER) estimator developed in this article to a range of realistic  $N$ -body simulations which are masked throughout by a pseudo-*Euclid* mask so as to best match upcoming Stage IV surveys.

### 5.1 Data set

Throughout this article, we perform reconstructions and uncertainty quantification on simulated convergence maps generated from the high resolution Takahashi  $N$ -body simulation data sets (Takahashi et al. 2017).<sup>6</sup> These mock convergence maps are generated via multiple-lens plane ray-tracing, and are provided for a range of comoving distances. Specifically, simulated convergence maps are presented at every  $150 \text{ Mpc h}^{-1}$  for redshift  $z_s \in [0.05, 5.3]$ . The cosmological parameters selected for this suite of simulations are

<sup>5</sup>In practice one may simply adjust  $\kappa^{\text{sur}}$  to suit a specific question of the posterior.

<sup>6</sup>These data sets can be found at [http://cosmo.phys.hirosaki-u.ac.jp/takahashi/allsky\\_raytracing/](http://cosmo.phys.hirosaki-u.ac.jp/takahashi/allsky_raytracing/).



$\Omega_m = 1$ ,  $\Omega_\Lambda = 0.279$ ,  $\Omega_{\text{cdm}} = 0.233$ ,  $\Omega_b = 0.046$ ,  $h = 0.7$ ,  $\sigma_8 = 0.82$ , and  $n_s = 0.97$  which are consistent with the *WMAP* 9 yr result (Hinshaw et al. 2013).

We select redshift slice 16 which corresponds to the slice with redshift  $z_s \sim 1$ . To mitigate the Poisson noise present in such  $N$ -body snapshots, we convolve the Takahashi convergence with a very small smoothing kernel sufficient only to remove the noise whilst adjusting the signal as little as possible. Finally we apply a pseudo-*Euclid* masking (a straightforward masking of the galactic plane and the ecliptic) so as to best mimic the setting of upcoming Stage IV surveys.

## 5.2 Methodology

As in previous work (Price et al. 2018, 2019a, b), we begin by applying the measurement operator  $\Phi$  (see equation 25) to the fiducial ground truth, full-sky Takahashi convergence map  $\kappa$  to create artificial masked clean shear measurements  $\gamma \in \mathbb{C}^M$ .

A noise standard deviation  $\sigma_i$  is computed (see Section 5.2.1) for each pixel  $i$  individually and used to construct known diagonal covariance  $\Sigma$ .<sup>7</sup> Hence we create noisy simulated shear observations  $\gamma_n = \gamma + n$  and a simulated data covariance  $\Sigma$  which would in practice be provided by the observation team – this covariance is defined by the number of galaxy observations within a given pixel of the sky.

We then apply the standard SKS estimator and the DARKMAPPER estimator presented in this paper to these noisy artificial measurements  $\gamma_n$  to create estimates of the fiducial convergence map  $\kappa$ . For DARKMAPPER, we simply adopt diadic axisymmetric spherical wavelets ( $N = 1$  and  $\lambda = 2$  for simplicity), with scale-discretized harmonic tiling (McEwen et al. 2018) (adopting minimum wavelet scale  $j_0 = 0$  and maximum wavelet scale  $j_{\text{max}} = 10$  resulting in a total of 11 wavelet scales). Additional complexity may produce better results at the cost of computational efficiency. Furthermore scale-discretized wavelets are only one possible choice of spherical wavelets (see Section 3.2.2). Other wavelets on the sphere could be adopted and are interchangeable within this reconstruction formalism, provided they support exact synthesis of a signal from its wavelet coefficients.

We adopt the signal-to-noise ratio (SNR) as a metric to compare how closely each convergence estimator matches the true convergence map. This recovered SNR in decibels (dB) is defined to be,

$$\text{Recovered SNR} = 20 \times \log_{10} \left( \frac{\|\kappa\|_2}{\|\kappa - \kappa^{\text{map}}\|_2} \right), \quad (43)$$

from which it is clear that the larger the recovered SNR the more accurate<sup>8</sup> the convergence estimator. Additionally we record the Pearson correlation coefficient between recovered convergence estimators  $\kappa^{\text{map}} \in \mathbb{C}^{N_{\text{S}^2}}$  and the fiducial convergence  $\kappa \in \mathbb{C}^{N_{\text{S}^2}}$  as a measure of topological fidelity of the estimator. The Pearson

<sup>7</sup>Note we here do not consider off diagonal terms which may arise due to intrinsic galaxy alignments though in future this can be incorporated straightforwardly.

<sup>8</sup>Accuracy here is in regard to the pixel-level deviation not structural correlation, for which specific estimators may be designed.

correlation coefficient is defined to be

$$r = \frac{\sum_{i=1}^{N_{\text{S}^2}} \{\kappa^{\text{map}}(i) - \bar{\kappa}^{\text{map}}\} \{\kappa(i) - \bar{\kappa}\}}{\sqrt{\sum_{i=1}^{N_{\text{S}^2}} \{\kappa^{\text{map}}(i) - \bar{\kappa}^{\text{map}}\}^2} \sqrt{\sum_{i=1}^{N_{\text{S}^2}} \{\kappa(i) - \bar{\kappa}\}^2}}, \quad (44)$$

where  $\bar{x} = \langle x \rangle$ . The correlation coefficient  $r \in [-1, 1]$  quantifies the structural similarity between two data sets: 1 indicates maximal positive correlation, 0 indicates no correlation, and  $-1$  indicates maximal negative correlation.

In practice the SKS estimator (as with its predecessor the KS estimator) is post-processed via axisymmetric convolution with an often quite large Gaussian smoothing kernel. The absolute scale of this kernel is typically chosen ‘by eye’ (which is to say arbitrarily), but in order to maximize the performance of the SKS estimator we iteratively compute the smoothing scale which maximizes the recovered SNR, yielding the best possible reconstruction that can be provided by the SKS estimator (i.e. with optimal smoothing). We then use this optimal SKS estimator for comparison. Note that this may only be performed in simulation settings where the fiducial convergence is known. Further note that such ad hoc parameters do not exist within the DARKMAPPER formalism, for which a principled statistical problem is posed and solved by automated optimization algorithms.

### 5.2.1 Noise

For weak-lensing surveys the noise level of a given pixel is dependent on: the number density of galaxy observations  $n_{\text{gal}}$  (typically given per arcmin<sup>2</sup>), the size of said pixel, and the variance of the intrinsic ellipticity distribution  $\sigma_e^2$ .

Knowing the area  $A$  of a given pixel the noise standard deviation  $\sigma_i$  is simply given by,

$$\sigma_i = \sqrt{\frac{\sigma_e^2}{A \times (180/\pi)^2 \times 3600 \times n_{\text{gal}}}}, \quad (45)$$

where  $3600(180/\pi)^2$  converts steradians to arcmin<sup>2</sup> – this relation is simply a reduction in the noise standard deviation by the root of the number of data points. Thus, larger pixels which (assuming a roughly uniform spatial distribution of galaxy observations) contain more observations have smaller noise variance. In practice the value of  $\sigma_i$  (and therefore the covariance  $\Sigma$ ) can be determined using the true number of galaxies in a given pixel rather than  $n_{\text{gal}}$ .

The typical intrinsic ellipticity standard deviation is  $\sigma_e \sim 0.37$ . Upcoming Stage IV surveys (e.g. *Euclid* (Laureijs et al. 2011) and LSST) are projected to achieve a number density of  $n_{\text{gal}} \sim 30$  arcmin<sup>-2</sup> – a soft limit due to blending complications. For academic discussion we also consider the case of a potential future space-based survey which may push the number density as high as  $n_{\text{gal}} \sim 100$  arcmin<sup>-2</sup>, in addition to lower number densities  $n_{\text{gal}} \in [5, 10]$  arcmin<sup>-2</sup> which are representative of past Stage III surveys.

## 5.3 Reconstruction results

For an angular band limit  $\ell_{\text{max}} = 2048$ , a pseudo-*Euclid* mask, and input  $n_{\text{gal}} \in [5, 10, 30, 100]$  we compute the spherical SKS estimator, an idealized (optimally smoothed) SKS estimator, and the DARKMAPPER estimator. The results can be found in Fig. 3 and numerically in Table 1. In all cases the DARKMAPPER estimator provides the highest reconstruction fidelity both in terms of recovered

## Ground Truth convergence

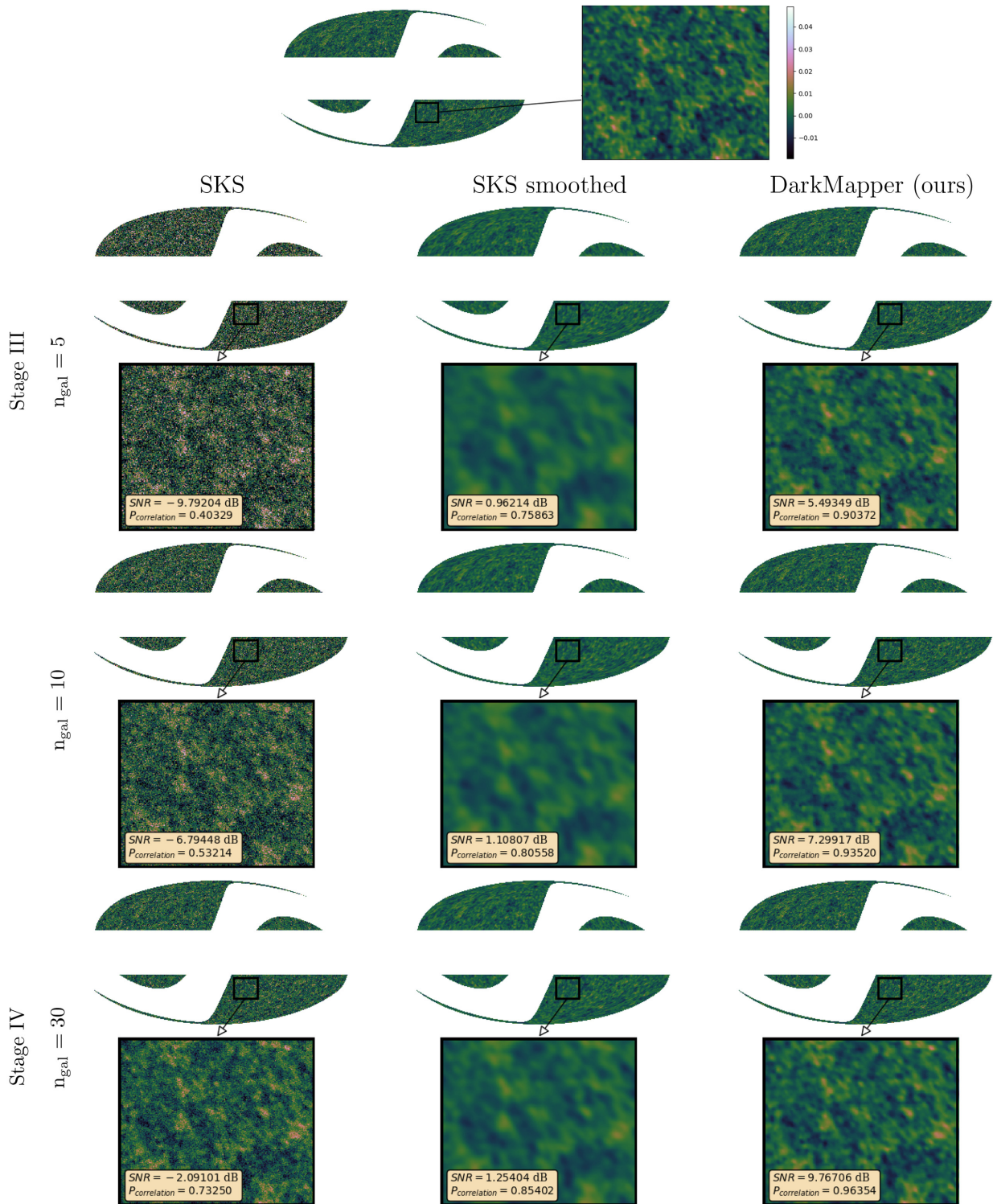


**Figure 3.** The top row displays the ground truth Takahashi convergence map as described in Section 5.1 with close up of a small region. Top to bottom: Increasing number density of galaxies ( $n_{\text{gal}}$ ) and therefore decreasing noise levels. At the top we have  $n_{\text{gal}} = 5$  which is representative of current Stage III surveys, at the bottom we have  $n_{\text{gal}} = 30$  which has been forecast for upcoming Stage IV surveys (e.g. *Euclid* / *LSST*). Left to right: The spherical Kaiser–Squires estimator without the ad hoc smoothing kernel post-processing, the optimally smoothed spherical Kaiser–Squires estimator, and finally the DARKMAPPER estimator. Discussion: Clearly the DARKMAPPER estimator is visibly superior in all cases, numerically recovering both significantly larger SNR and Pearson correlation coefficients. All reconstructions are plotted on the same colourscale to aid comparison (Green 2011).

**Table 1.** Numerical results from reconstructions of Takahashi simulations as discussed in Sections 5.1 and 5.2. In each case the DARKMAPPER estimator drastically outperforms both the SKS estimator and the optimally smoothed SKS estimator (which cannot in practice be achieved due to ad hoc smoothing kernel selection) in both recovered signal-to-noise ratio (SNR) and the Pearson correlation coefficient  $P_{\text{correlation}}$ . Highlighted are the results most representative of the imminent Stage IV surveys, such as *Euclid* and *LSST*. As Stage IV surveys forecast large sky fractions to avoid projection effects (Wallis et al. 2017a; Vallis et al. 2018) mass-mapping must be performed natively on the sphere. Thus this spherical mass-mapping formalism is, at least currently, the optimal choice for Stage IV weak lensing mass-mapping. Note that no post-processing by smoothing increased the recovered SNR for the idealized  $n_{\text{gal}} = 100$  setting for the SKS estimator and so was recorded as n/a.

$\ell_{\text{max}} = 2048$		SKS		SKS (optimal smoothing)		DARKMAPPER		Difference
Setting	$n_{\text{gal}}$	SNR (dB)	$P_{\text{correlation}}$	SNR (dB)	$P_{\text{correlation}}$	SNR (dB)	$P_{\text{correlation}}$	$\Delta$ SNR (dB)
Stage III	5	-9.792	0.403	0.962	0.759	5.494	0.904	+15.286 (+4.532)
	10	-6.794	0.532	1.108	0.806	7.299	0.935	+14.093 (+6.191)
Stage IV	30	-2.091	0.732	1.254	0.854	9.767	0.964	+11.858 (+8.513)
Idealized	100	2.956	0.887	n/a	n/a	12.132	0.980	+9.176 (n/a)

SNR and Pearson correlation coefficient. Note that for  $\ell_{\text{max}} = 2048$  and the number density of galaxy observations selected the mean number of galaxies per pixel is  $\mathcal{O}(10 - 10^3)$ .

It is important to note that the optimal smoothing kernel for the SKS estimator cannot be known and thus in practice is often selected ‘by eye’ which is to say selected ad hoc. Therefore the smoothed SKS results here constitute an upper bound. The DARKMAPPER framework is fully principled and requires no ad hoc parameter selection and is therefore likely to perform in much the same way when applied to observational data.

For Stage III survey settings with  $n_{\text{gal}} = 5, 10$  the increase in SNR ( $\Delta$  SNR) of the DARKMAPPER estimator over the SKS (optimally smoothed SKS) estimator was +15.286 (+4.532) dB and +14.093 (+6.191) dB, respectively. Recall that dB is measured on a logarithmic scale (see equation 43) and so this increase is quite dramatic. Furthermore, the Pearson correlation coefficient increased from 0.403 (0.759) to 0.904 and 0.532 (0.860) to 0.935 for  $n_{\text{gal}} = 5, 10$ , respectively.

For the Stage IV *Euclid*-type setting with  $n_{\text{gal}} = 30$   $\Delta$ , SNR was found to be +11.858 (+8.513) dB, along with which the Pearson correlation coefficient rose from 0.723 (0.854) to 0.964. As this setting is highly representative of the observations which will be made in Stage IV surveys, this strongly suggests that algorithms such as DARKMAPPER should be adopted for weak lensing mass-mapping.

## 6 APPLICATION TO PUBLIC DATA

Finally, we apply both the SKS and DARKMAPPER estimators to a collated map of the majority of the public wide-field weak lensing observational data sets in order to reconstruct a single global dark-matter mass-map computed natively on the sphere. Furthermore, we demonstrate straightforward global uncertainty quantification on our reconstruction.

Specifically, we perform convergence reconstructions on the DESY1 (Flaugher et al. 2015; Abbott et al. 2018; Morganson et al. 2018), CFHTLens (Erben et al. 2012), and the KiDS450 (Fenech Conti et al. 2017; Hildebrandt et al. 2017) weak lensing shear data sets. See specific acknowledgements and related papers for further details. Note that throughout we have not chosen to perform reduced shear iterations, assuming that the observed shear is approximately the reduced shear  $\gamma \sim g$  (in a more detailed analysis one could perform such further iterations)

### 6.1 Joint spherical mass-map

All aforementioned weak lensing shear observational data sets were collated into a single joint global data set. For each data set we select only galaxies with non-zero catalogue weight  $w(i) > 0$  and perform a correction for the multiplicative bias by  $w(i)$  and additive by  $c_{1,2}(i)$  biases per observation. Specifically this correction for ellipticities  $e_{1,2}(i)$  is given by

$$\begin{aligned}\Re\{\gamma(i)\} &= \frac{\sum_j w(j)\{e_1(j) - c_1(j)\}}{\sum_j w(j)\{1 + \text{mcorr}(j)\}}, \\ \Im\{\gamma(i)\} &= \frac{\sum_j w(j)\{e_2(j) - c_2(j)\}}{\sum_j w(j)\{1 + \text{mcorr}(j)\}},\end{aligned}\quad (46)$$

where  $j$  are observations such that observation  $j$  belongs to pixel  $i$ ,  $\text{mcorr}$  is the catalogue magnification correction, and  $\Re, \Im$  denote the real and imaginary components of the shear field  $\boldsymbol{\gamma}$ , respectively.

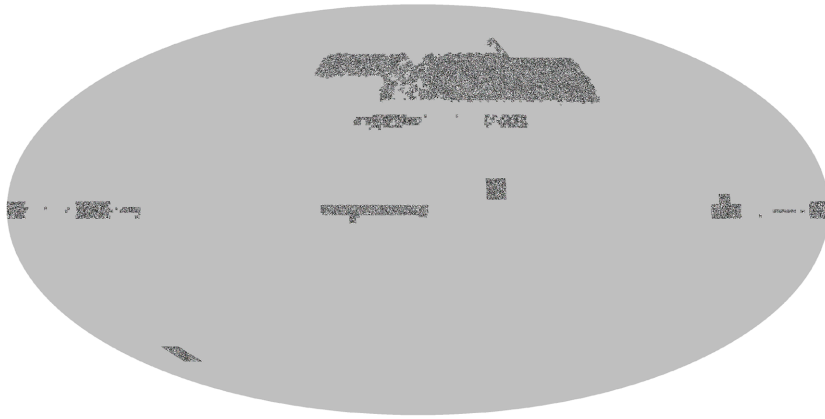
This joint global data set was then projected on to an equiangularly sampled (MW) spherical shear map  $\gamma_{\text{obs}}$  with an angular band limit of  $\ell_{\text{max}} = 2048$ . During this projection the number of galaxies projected into each pixel was recorded to create a complementary map of observations per pixel, from which the data covariance  $\Sigma_{\text{obs}}$  is directly determined (as discussed in Sections 3.2.1 and 5.2.1)

To this spherical shear map  $\gamma_{\text{obs}}$  (with corresponding data covariance  $\Sigma_{\text{obs}}$ ) we apply DARKMAPPER outlined in Section 3 with the same parameter choices outlined in Section 5 (see Price et al. 2018, for a planar equivalent). Additionally, we provide the SKS (Wallis et al. 2017a) reconstruction which we present in both its fundamental form (without post-processing Gaussian smoothing) and in its typical form (with post-processing Gaussian smoothing with full-width at half-maximum FWHM =  $\Theta = 25$  arcmin). All data products aforementioned within this section are publicly available and may be found at <https://doi.org/10.5281/zenodo.3980652>.

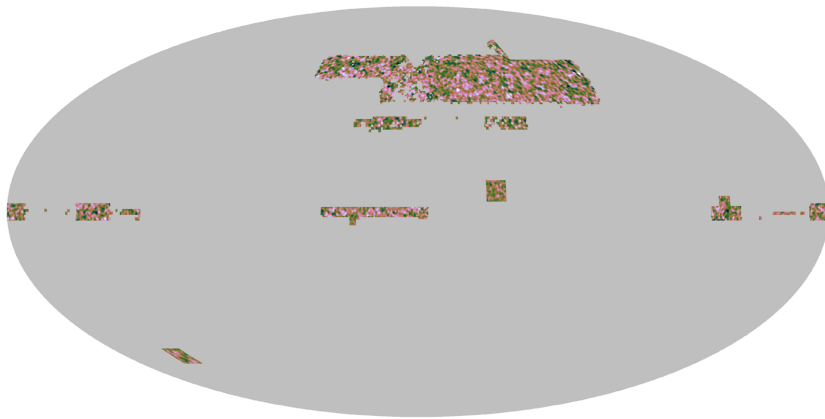
The results of all reconstruction algorithms can be seen globally in Fig. 4 and with enhanced regions in Fig. 5, where all subplots share the same colourscale (Green 2011). It is immediately apparent that the SKS estimator, in the absence of smoothing, is overwhelming dominated by noise (hence the motivation for post-processing).

In contrast to this, the SKS estimator with a  $\Theta = 25$  arcmin post-processing Gaussian smoothing is largely in agreement with the DARKMAPPER estimator, however this smoothed SKS estimator unsurprisingly lacks any significant small-scale structure. Further note that the smoothed SKS estimator does not mirror all high-

SKS



SKS smoothed



DarkMapper (ours)

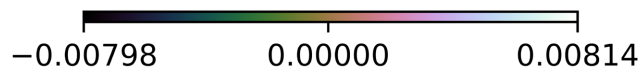
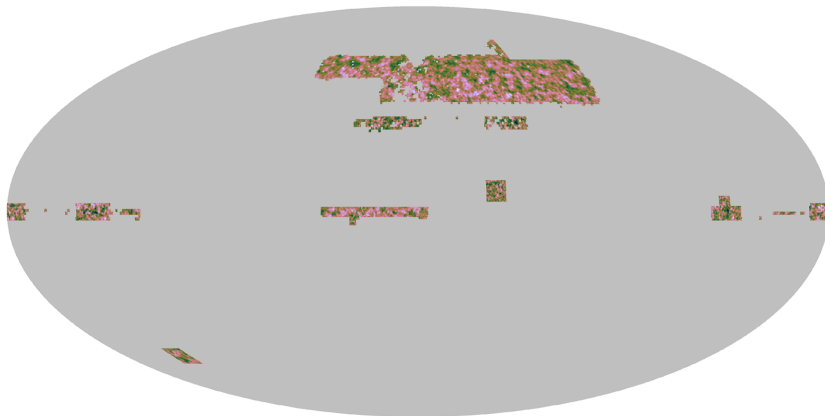


**Figure 4.** Mollweide projections of global reconstruction of the majority of public weak lensing data sets. Top to bottom: Spherical Kaiser–Squires (SKS) estimator without Gaussian smoothing kernel, SKS estimator with  $\text{FWHM} = \Theta = 25$  arcmin smoothing kernel (as in other studies), DARKMAPPER (our) estimator. All reconstructions are plotted on the same colourscale to aid comparison (Green 2011). The data sets can be found online at <https://doi.org/10.5281/zenodo.3980652>.

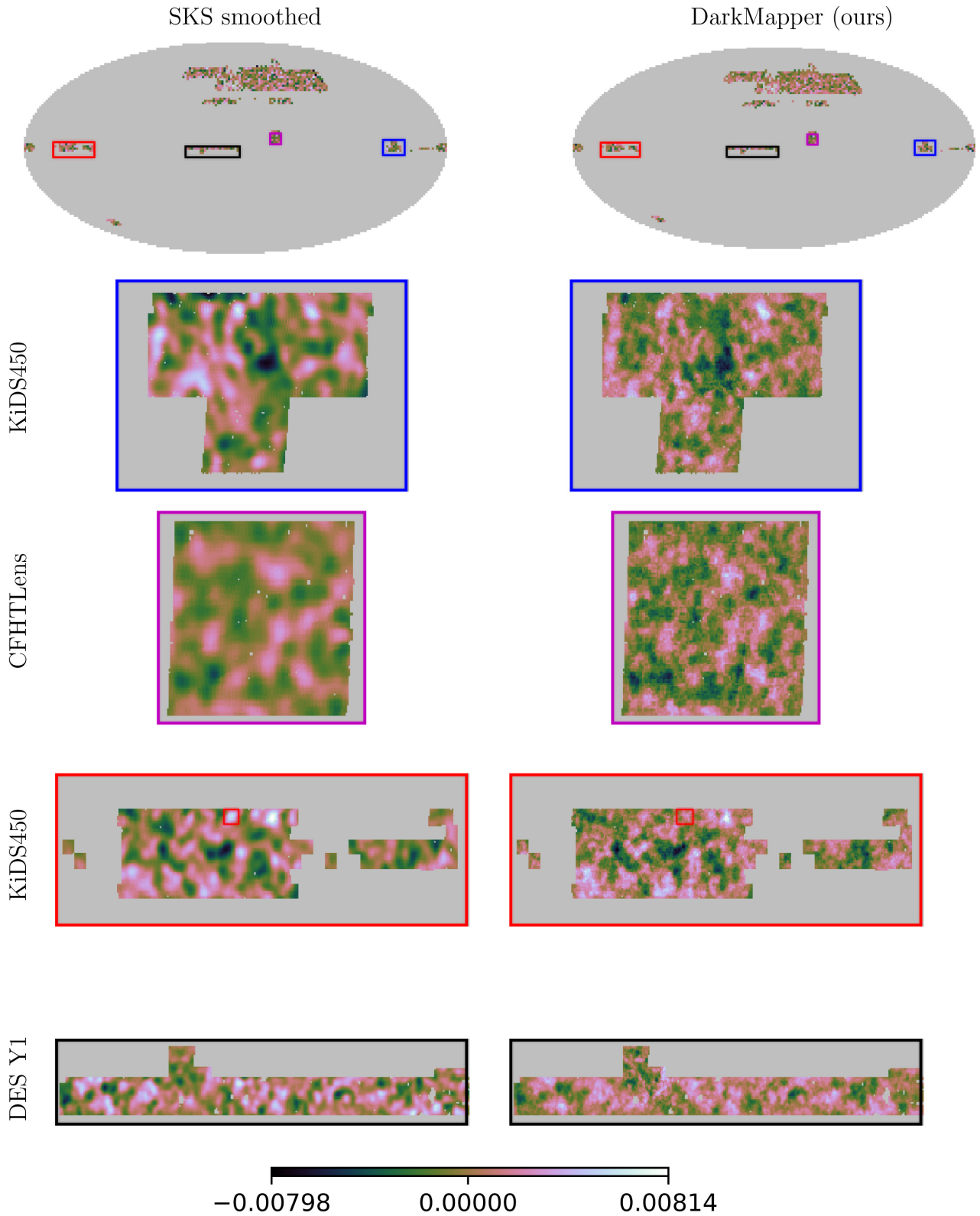


**Figure 5.** Top to bottom: Global reconstruction of the majority of public weak lensing data sets, magnified view of a variety of patches. Left to right: Spherical Kaiser–Squires (SKS) estimator without Gaussian smoothing kernel, SKS estimator with  $\text{FWHM} = \Theta = 25$  arcmin smoothing kernel (as in other studies), DARKMAPPER (our) estimator. Discussion: Note the overall agreement between both the smoothed SKS estimator and our DARKMAPPER estimator, however notice the significant increase in small-scale detail captured by the DARKMAPPER estimator. All reconstructions are plotted on the same colourscale to aid comparison (Green 2011). These data sets can be found online at <https://doi.org/10.5281/zenodo.3980652>.

**Table 2.** Description: Uncertainty quantification of convergence estimators and smoothing scales, in each case the convergence surrogate solution  $\kappa^{\text{sur}}$  is defined by estimator (i.e. SKS) and Gaussian smoothing scale  $\text{FWHM} = \Theta$  in arcmin. For each surrogate both the objective function and the ratio of the objective function to the level set threshold at 99 per cent confidence  $\epsilon'_{99\text{ per cent}}$  is presented. The right-hand column indicates whether a given surrogate  $\kappa^{\text{sur}}$  belongs to the credible set (and is therefore not rejected as a possible solution to the reconstruction). Shaded in red are solutions which are rejected by Bayesian hypothesis testings. Discussion: Clearly, the SKS estimator without smoothing is unequivocally rejected, which is concurrent with the community’s intuition that smoothing is required for the SKS estimator to produce physically meaningful solutions. The minimal smoothing scale required for any SKS solution to not be rejected is  $\Theta \sim 15$  arcmin, therefore with a typical smoothing of  $\Theta \in [25, 30]$  arcmin the SKS solution belongs to the DARKMAPPER credible set and cannot be rejected at 99 per cent confidence (i.e. the two estimators are not necessarily conflicting). Nevertheless, the DARKMAPPER estimator contains greater fine-scale structure.

Surrogate $\kappa^{\text{sur}}$		Analysis ( $\epsilon'_{99\text{ per cent}} = 842789$ )		Hypothesis test
Estimator	$\Theta$ (arcmin)	$\text{Obj}(\kappa^{\text{sur}})$	$\text{Obj}(\kappa^{\text{sur}})/\epsilon'_{99\text{ per cent}}$	$\kappa^{\text{sur}} \in C'_{99\text{ per cent}}$
SKS	0	6151070	7.298	✗
	5	2584510	3.067	✗
	10	891266	1.058	✗
	15	586741	0.696	✓
	20	513223	0.609	✓
	25	488887	0.580	✓
	30	478245	0.567	✓

intensity structure (e.g. peaks and voids) recovered by the DARKMAPPER estimator, which indicates more significant deviations between the two estimators. The most egregious of these cases is highlighted in the red boxed KiDS450 patch of Fig. 5.

These structural dissimilarities between the smoothed SKS and DARKMAPPER estimator may reasonably be attributed to large noise fluctuations and boundary effects, both of which are not reasonably accounted for by the SKS estimator. Observation of such significant differences indicates that more principled reconstruction algorithms (such as DARKMAPPER) are important considerations when attempting to perform future statistical and scientific inference from dark matter mass-maps.

All reconstructions were performed on a 2016 MacBook air and took  $\sim 30$  h to compute. A further  $\sim 100$  h were optionally undertaken for annealing iterations to optimize the convergence. Note that this is by no means a benchmark of computational performance.

## 6.2 Local uncertainty quantification

Given significant structural dissimilarities between the SKS and DARKMAPPER convergence estimators we performed several hypothesis tests of local structure. Specifically, we addressed the missing peaks observed in the smoothed SKS estimator of the lower (red) region of Fig. 5 but not in the corresponding DARKMAPPER estimator. We did so by performing local hypothesis testing of structure as described in Section 4.2.1 (see Price et al. 2018, for more comprehensive details).

In all cases the hypothesis test of local structure could not reject the existence of such structure at reasonable confidence. This is unsurprising given the notably high noise level inherent to Stage III weak lensing surveys (which reduces the magnitude of the objective function, thus making the approximate level set threshold  $\epsilon'_\alpha$  more difficult to reach; see Section 4) and the extremely high dimensionality  $\sim \mathcal{O}(10^7)$  of the reconstruction (which directly increases the level set threshold  $\epsilon'_\alpha$  in equation 40).

## 6.3 Global uncertainty quantification

For high dimensional cases it is often more informative to consider global features of the reconstruction, as discussed in Section 4.

A question one may wish to address is for which smoothing scales  $\Theta$  does the SKS estimator provide solutions that are not in disagreement with the DARKMAPPER estimator at some well defined confidence.

To address this question within our global uncertainty quantification, we consider the SKS estimator with a variety of Gaussian smoothing kernels, specifically  $\Theta = 5i$  for integer  $i \in [0, 6]$ , which is to say a uniform sampling of different (in practice arbitrary) smoothing choices ranging from no smoothing (the basic SKS estimator) to the typically adopted case of  $\Theta \sim 30$  arcmin smoothing. In this way we can directly address the question of which smoothing scales produces solutions  $\kappa^{\text{sur}}(\Theta)$  belong to the DARKMAPPER approximate HPD-credible region  $C'_\alpha$  (are consistent with the DARKMAPPER estimator) and which solutions are unacceptable (i.e. those solutions which reject the null hypothesis that the surrogate is within the credible set) at  $100(1 - \alpha)$  per cent confidence.

The results of this global uncertainty quantification (at 99 per cent confidence) can be found numerically in Table 2. Despite the high noise level present in the joint data set, the uncertainty quantification technique is sensitive enough to reject the SKS estimator for  $\Theta = 0, 5, 10$  arcmin, which is to say that these smoothing scales are in disagreement with the DARKMAPPER estimator at 99 per cent confidence and are unlikely to be physically meaningful. This provides statistically rigorous evidence for the community’s intuition that SKS estimators require considerable smoothing to be considered meaningful.

This raises an interesting point worth noting: the SKS estimator (by construction) locates solutions within  $C'_\alpha$  which exhibit relatively little small-scale structure, whereas the DARKMAPPER estimator locates solutions within  $C'_\alpha$  which retain significantly greater small-scale structure. Therefore, though the two solutions do not disagree at  $100(1 - \alpha)$  per cent confidence, the DARKMAPPER estimator places relatively more probability on small-scale structures.

Note that if both estimators provided details of the HPD credible set then a stronger discussion of the relative cardinality of the intersection of both HPD credible sets could be used to quantify the level of statistical agreement. However, in this case the SKS estimator does not support a principled statistical interpretation and so can only justifiably be treated as a point estimate.

## 7 CONCLUSIONS

In this paper, we have extended the previously presented (Price et al. 2018) sparse Bayesian reconstruction formalism to the spherical setting, resulting in a sparse spherical Bayesian mass-mapping algorithm which we refer to as DARKMAPPER. This algorithm is general and accommodates any log-concave posterior. In this paper, we adopt a Laplace-type sparsity promoting wavelet prior with a multivariate Gaussian likelihood.

The DARKMAPPER mass-mapping algorithm was benchmarked against spherical Kaiser–Squires (Wallis et al. 2017a) in a variety of realistic weak lensing settings (ranging from Stage III to future space-based surveys) using the Takahashi (Takahashi et al. 2017)  $N$ -body simulations and a pseudo-*Euclid* masking. In all cases we perform analysis at a typically adopted angular band limit of  $\ell_{\max} = 2048$ . We do not consider intrinsic alignments in this paper, but highlight how they may be included should one wish it.

In all simulations the DARKMAPPER algorithm dramatically outperforms (in both recovered SNR and recovered Pearson correlation coefficient) the SKS estimator, even when artificially selecting the optimal SKS smoothing kernel (i.e. even when biasing our evaluation in favour of SKS as strongly as possible).

We extend approximate Bayesian uncertainty quantification methods (Pereyra 2017; Cai et al. 2018b; Price et al. 2018, 2019a, b; Repetti, Pereyra & Wiaux 2018) to the spherical setting and explain how one may leverage these methods from local uncertainty quantification to general global (or aggregate) uncertainty quantification.

The DARKMAPPER estimator was applied to a joint observational shear data set constructed by collating the majority of publicly available weak lensing data – specifically the DESY1 (Flaugher et al. 2015; Abbott et al. 2018; Morganson et al. 2018), CFHTLenS (Erben et al. 2012), and the KiDS450 (Fenech Conti et al. 2017; Hildebrandt et al. 2017) surveys. To the best of our knowledge, this is the first joint spherical reconstruction of all public weak lensing shear observations.

For comparison we also computed the SKS estimator of this joint data set. We find, as with the simulated benchmarking, that the DARKMAPPER algorithm recovers significantly more fine-scale structure without the need for any assumptions of Gaussianity or ad hoc smoothing parameters (i.e. the smoothing scale for SKS post-processing). This demonstrates that the algorithm works as expected on observational data.

Finally, uncertainty quantification was carried out to determine for which smoothing scales the SKS point estimates provide solutions that are acceptable solutions to the DARKMAPPER Bayesian inference problem (i.e. within the highest posterior density credible region) – this is to say the smoothing scales at which both convergence estimates are not conflicting at 99 per cent confidence. It was found that all SKS reconstructions with smoothing scales below  $\sim 15$  arcmin were rejected at 99 per cent confidence, indicating that significant smoothing is required for agreement between the SKS and DARKMAPPER estimators. This reaffirms the community’s understanding that SKS estimators must undergo significant smoothing to recover physically meaningful convergence maps.

Moreover, we demonstrate that the DARKMAPPER estimator locates permissible solutions with significantly greater small-scale structure than those which are located by the SKS estimator. More constraining statistical statements were limited by the inherently high noise level in current observational shear data.

With the advent of Stage IV surveys the pixel noise level is projected to drop dramatically (due to increased galaxy number density), which will inevitably facilitate significantly more constrain-

ing statistical statements. As the DARKMAPPER estimator not only provides dramatically increased reconstruction fidelity over the SKS estimator but also supports a principled Bayesian interpretation, it will be of important use for application to Stage IV data sets.

Note that just as we have extended this sparse hierarchical Bayesian mass-mapping formalism to the sphere ( $S^2$ ) one can extend it to the ball ( $B^3$ ) and thus recover similar results for the case of full 3D mass-mapping. This is a possible avenue for future investigation.

## ACKNOWLEDGEMENTS

The authors would like to thank the development teams of S2INV (Price et al., in preparation), SOPT (Carrillo et al. 2012, 2013; Onose et al. 2016; Pratley et al. 2018)<sup>9</sup> SSHT (McEwen & Wiaux 2011; McEwen et al. 2013a),<sup>10</sup> S2LET (McEwen & Wiaux 2011; Leistedt et al. 2013; McEwen et al. 2015a, b; Chan et al. 2017; McEwen et al. 2018),<sup>11</sup> and SO3 (McEwen et al. 2015a)<sup>12</sup> upon which this work is built. Additionally the authors would like to thank Dr. Peter Taylor for providing the pseudo-*Euclid* mask and Dr. Xiaohao Cai for insightful discussion.

MAP is supported by the Science and Technology Facilities Council (STFC). TDK is supported by a Royal Society University Research Fellowship (URF). This work was also supported by the Engineering and Physical Sciences Research Council (EPSRC) through grant EP/M0110891 and by the Leverhulme Trust. The Dunlap Institute is funded through an endowment established by the David Dunlap family and the University of Toronto.

DES acknowledgements: This project used public archival data from the Dark Energy Survey (DES). Funding for the DES Projects has been provided by the U.S. Department of Energy, the U.S. National Science Foundation, the Ministry of Science and Education of Spain, the Science and Technology Facilities Council of the United Kingdom, the Higher Education Funding Council for England, the National Center for Supercomputing Applications at the University of Illinois at Urbana-Champaign, the Kavli Institute of Cosmological Physics at the University of Chicago, the Center for Cosmology and Astro-Particle Physics at the Ohio State University, the Mitchell Institute for Fundamental Physics and Astronomy at Texas A&M University, Financiadora de Estudos e Projetos, Fundação Carlos Chagas Filho de Amparo à Pesquisa do Estado do Rio de Janeiro, Conselho Nacional de Desenvolvimento Científico e Tecnológico and the Ministério da Ciência, Tecnologia e Inovação, the Deutsche Forschungsgemeinschaft, and the Collaborating Institutions in the Dark Energy Survey.

The Collaborating Institutions are Argonne National Laboratory, the University of California at Santa Cruz, the University of Cambridge, Centro de Investigaciones Energéticas, Medioambientales y Tecnológicas-Madrid, the University of Chicago, University College London, the DES-Brazil Consortium, the University of Edinburgh, the Eidgenössische Technische Hochschule (ETH) Zürich, Fermi National Accelerator Laboratory, the University of Illinois at Urbana-Champaign, the Institut de Ciències de l’Espai (IEEC/CSIC), the Institut de Física d’Altes Energies, Lawrence Berkeley National Laboratory, the Ludwig-Maximilians Universität München and the associated Excellence Cluster Universe, the University of Michigan, the National Optical Astronomy Observatory, the University

<sup>9</sup><https://github.com/astro-informatics/sopt>

<sup>10</sup><https://astro-informatics.github.io/ssht/>

<sup>11</sup><http://astro-informatics.github.io/s2let/>

<sup>12</sup><http://astro-informatics.github.io/so3/>

of Nottingham, The Ohio State University, the OzDES Membership Consortium, the University of Pennsylvania, the University of Portsmouth, SLAC National Accelerator Laboratory, Stanford University, the University of Sussex, and Texas A&M University.

Based in part on observations at Cerro Tololo Inter-American Observatory, National Optical Astronomy Observatory, which is operated by the Association of Universities for Research in Astronomy (AURA) under a cooperative agreement with the National Science Foundation.

Kilo degree survey acknowledgements: Based on data products from observations made with ESO Telescopes at the La Silla Paranal Observatory under programme IDs 177.A-3016, 177.A-3017 and 177.A-3018.

We use cosmic shear measurements from the Kilo-Degree Survey (Kuijken et al. 2015; Fenech Conti et al. 2017; Hildebrandt et al. 2017), hereafter referred to as KiDS. The KiDS data are processed by THELI (Erben et al. 2013) and Astro-WISE (McFarland et al. 2013; de Jong et al. 2015). Shears are measured using lensfit (Miller et al. 2013), and photometric redshifts are obtained from PSF-matched photometry and calibrated using external overlapping spectroscopic surveys (see Hildebrandt et al. 2017).

## DATA AVAILABILITY

All observational data utilized throughout this paper is publicly available and can be found in the corresponding references. All joint reconstruction data sets are publicly available and can be found online at <https://doi.org/10.5281/zenodo.3980652>. The DARKMAPPER reconstruction software will be publicly released in the near future.

## REFERENCES

- Abbott T. M. C. et al., 2018, *ApJS*, 239, 18
- Alsing J., Kirk D., Heavens A., Jaffe A. H., 2015, *MNRAS*, 452, 1202
- Alsing J., Heavens A., Jaffe A. H., Kiessling A., Wandelt B., Hoffmann T., 2016, *MNRAS*, 455, 4452
- Baldi P. et al., 2009, *Ann. Stat.*, 37, 1150
- Barreiro R. B., Hobson M. P., Lasenby A. N., Banday A. J., Górski K. M., Hinshaw G., 2000, *MNRAS*, 318, 475
- Bartelmann M., Schneider P., 2001, *Phys. Rep.*, 340, 291
- Bunn E. F., Zaldarriaga M., Tegmark M., de Oliveira-Costa A., 2003, *Phys. Rev. D*, 67, 023501
- Cai X., Pereyra M., McEwen J. D., 2018a, *MNRAS*, 480, 4154
- Cai X., Pereyra M., McEwen J. D., 2018b, *MNRAS*, 480, 4170
- Carrillo R. E., McEwen J. D., Wiaux Y., 2012, *MNRAS*, 426, 1223
- Carrillo R. E., McEwen J. D., Van De Ville D., Thiran J.-P., Wiaux Y., 2013, *IEEE Signal Process. Lett.*, 20, 591
- Castro P. G., Heavens A. F., Kitching T. D., 2005, *Phys. Rev. D*, 72, 023516
- Chan J. Y. H., Leistedt B., Kitching T. D., McEwen J. D., 2017, *IEEE Trans. Signal Process.*, 65, 5
- Chang C. et al., 2018, *MNRAS*, 475, 3165
- Clowe D., Bradač M., Gonzalez A. H., Markevitch M., Randall S. W., Jones C., Zaritsky D., 2006, *ApJ*, 648, L109
- Coles P., Chiang L.-Y., 2000, *Nature*, 406, 376
- Combettes P. L., Pesquet J.-C., 2009, preprint ([arXiv:0912.3522](https://arxiv.org/abs/0912.3522))
- Corless V. L., King L. J., Clowe D., 2009, *MNRAS*, 393, 1235
- de Jong J. T. A. et al., 2015, *A&A*, 582, A62
- Erben T. et al., 2012, *MNRAS*, 433, 146
- Erben T. et al., 2013, *MNRAS*, 433, 2545
- Fenech Conti I., Herbonnet R., Hoekstra H., Merten J., Miller L., Viola M., 2017, *MNRAS*, 467, 1627
- Flaugher B. et al., 2015, *AJ*, 150, 150
- Fluri J., Kacprzak T., Sgier R., Refregier A., Amara A., 2018, *J. Cosmol. Astropart. Phys.*, 2018, 051
- Fluri J., Kacprzak T., Lucchi A., Refregier A., Amara A., Hofmann T., Schneider A., 2019, *Phys. Rev. D*, 100, 063514
- Giblin B. et al., 2018, *MNRAS*, 480, 5529
- Goldberg J. N., Macfarlane A. J., Newman E. T., Rohrlach F., Sudarshan E. C. G., 1967, *J. Math. Phys.*, 8, 2155
- Green D. A., 2011, *Bull. Astron. Soc. India*, 39, 289
- Grimm N., Yoo J., 2018, *J. Cosmol. Astropart. Phys.*, 2018, 067
- Hildebrandt H. et al., 2017, *MNRAS*, 465, 1454
- Hinshaw G. et al., 2013, *ApJS*, 208, 19
- Horowitz B., Seljak U., Aslanyan G., 2019, *J. Cosmol. Astropart. Phys.*, 2019, 035
- Jee M. J., Dawson W. A., Stroe A., Wittman D., van Weeren R. J., Brügger M., Bradač M., Röttgering H., 2016, *ApJ*, 817, 179
- Jeffrey N. et al., 2018, *MNRAS*, 479, 2871
- Kaiser N., Squires G., 1993, *ApJ*, 404, 441
- Kuijken K. et al., 2015, *MNRAS*, 454, 3500
- Lanusse F., Starck J.-L., Leonard A., Pires S., 2016, *A&A*, 591, A2
- Laureijs R. et al., 2011, preprint ([arXiv:1110.3193](https://arxiv.org/abs/1110.3193))
- Leistedt B., McEwen J. D., Vanderghaynst P., Wiaux Y., 2013, *A&A*, 558, A128
- Mallat S., 1999, *A Wavelet Tour of Signal Processing*, Elsevier
- Marinucci D. et al., 2007, *MNRAS*, 383, 539
- McEwen J. D., Price M. A., 2019, in 27th European Signal Processing Conference (EUSIPCO), preprint ([arXiv:1510.01595](https://arxiv.org/abs/1510.01595))
- McEwen J. D., Scaife A. M. M., 2008, *MNRAS*, 389, 1163
- McEwen J. D., Wiaux Y., 2011, *IEEE Trans. Signal Process.*, 59, 5876
- McEwen J. D., Wiaux Y., Eyers D. M., 2011, *A&A*, 531, A98
- McEwen J. D., Puy G., Thiran J.-P., Vanderghaynst P., Van De Ville D., Wiaux Y., 2013a, *IEEE Trans. Image Process.*, 22, 2275
- McEwen J. D., Vanderghaynst P., Wiaux Y., 2013b, in Van De Ville D., Goyal V. K., Papadakis M., eds, Proc. SPIE Conf. Ser. Vol. 8858, Wavelets and Sparsity XV. SPIE, Bellingham, p. 88580I
- McEwen J. D., Leistedt B., Büttner M., Peiris H. V., Wiaux Y., 2015a, preprint ([arXiv:1509.06749](https://arxiv.org/abs/1509.06749))
- McEwen J. D., Büttner M., Leistedt B., Peiris H. V., Wiaux Y., 2015b, *IEEE Signal Process. Lett.*, 22, 2425
- McEwen J. D., Durastanti C., Wiaux Y., 2018, *Appl. Comput. Harmonic Anal.*, 44, 59
- McFarland J. P., Verdoes-Kleijn G., Sikkema G., Helmich E. M., Boxhoorn D. R., Valentijn E. A., 2013, *Exp. Astron.*, 35, 45
- Mediavilla E., Muñoz J. A., Garzón F., Mahoney T. J., 2016, *Astrophysical Applications of Gravitational Lensing*, Cambridge Univ. Press, Cambridge
- Miller L. et al., 2013, *MNRAS*, 429, 2858
- Moreau J. J., 1962, *C.R. Acad. Sci. Paris Ser. A Math.*, 255, 2897
- Morganson E. et al., 2018, *PASP*, 130, 074501
- Munshi D., Coles P., 2017, *J. Cosmol. Astropart. Phys.*, 2017, 010
- Narcowich F. J., Petrushev P., Ward J. D., 2006, *SIAM J. Math. Anal.*, 38, 574
- Newman E. T., Penrose R., 1966, *J. Math. Phys.*, 7, 863
- Onose A., Carrillo R. E., Repetti A., McEwen J. D., Thiran J.-P., Pesquet J.-C., Wiaux Y., 2016, *MNRAS*, 462, 4314
- Peel A., Pettorino V., Giocoli C., Starck J.-L., Baldi M., 2018, *A&A*, 619, A38
- Pereyra M., 2017, *SIAM J. Imaging Sci.*, 10, 285
- Pereyra M., Bioucas-Dias J., Figueiredo M., 2015, 23rd European Signal Processing Conference (EUSIPCO). IEEE, p. 230
- Pichon C., Thiébaud E., Prunet S., Benabed K., Colombi S., Sousbie T., Teyssier R., 2010, *MNRAS*, 401, 705
- Planck Collaboration VI, 2020, *A&A*, 641, A6
- Pratley L., McEwen J. D., d’Avezac M., Carrillo R. E., Onose A., Wiaux Y., 2018, *MNRAS*, 473, 1038
- Price M. A., Cai X., McEwen J. D., Kitching T. D., Wallis C. G. R., 2018, preprint ([arXiv:1812.04014](https://arxiv.org/abs/1812.04014))
- Price M. A., McEwen J. D., Cai X., Kitching T. D., 2019a, *MNRAS*, 489, 3236
- Price M. A., Cai X., McEwen J. D., Pereyra M., Kitching T. D., 2019b, *MNRAS*, 492, 394



- Repetti A., Pereyra M., Wiaux Y., 2019, *SIAM J. Imaging Sci.*  
 Robert C.-P., 2001, *The Bayesian Choice*, Springer, New York, NY  
 Schneider P., 2005, *Gravitational Lensing: Strong, Weak and Micro: SAAS-FEE, Vol. 33*. Springer, Berlin, Heidelberg, p. 269  
 Schneider M. D., Hogg D. W., Marshall P. J., Dawson W. A., Meyers J., Bard D. J., Lang D., 2015, *ApJ*, 807, 87  
 Schröder P., Sweldens W., 1995, in *Computer Graphics Proceedings (SIGGRAPH '95)*, p. 161  
 Starck J.-L., Moudden Y., Abrial P., Nguyen M., 2006, *A&A*, 446, 1191  
 Takahashi R., Hamana T., Shirasaki M., Namikawa T., Nishimichi T., Osato K., Shiroyama K., 2017, *ApJ*, 850, 24  
 Taylor P. L., Kitching T. D., McEwen J. D., 2018, *Phys. Rev. D*, 98, 043532  
 Trotta R., 2017, preprint (arXiv:1701.01467)  
 Vallis Z. M., Wallis C. G. R., Kitching T. D., 2018, *Astron. Comput.*, 24, 84  
 Van Waerbeke L. et al., 2013, *MNRAS*, 433, 3373  
 VanderPlas J. T., Connolly A. J., Jain B., Jarvis M., 2011, *ApJ*, 727, 118  
 Wallis C. G. R., McEwen J. D., Kitching T. D., Leistedt B., Plouviez A., 2017a, preprint (arXiv:1703.09233)  
 Wallis C. G. R., Wiaux Y., McEwen J. D., 2017b, *IEEE Trans. Image Process.*, 26, 5176  
 Wiaux Y., McEwen J. D., Vandergheynst P., Blanc O., 2008, *MNRAS*, 388, 770

## APPENDIX A: WAVELETS ON THE SPHERE

This section will provide extremely brief (and quite technical) overview of scale-discretized spherical wavelets; for extensive details see the related articles (Wiaux et al. 2008; Leistedt et al. 2013; McEwen et al. 2013a, 2015a, b, 2018; McEwen & Price 2019; Chan et al. 2017; Wallis et al. 2017b).

The scale-discretized wavelet transform on the sphere is given by the directional convolution of each wavelet  $\Psi^j$  of scale  $j \in [J_0, J_{\max}]$  with a field  ${}_0\kappa$ , such that the wavelet coefficients  $w^j(\rho) \in \ell^2_{\max}(\text{SO}(3))$  are given by,

$$w^j(\rho) = \int_{S^2} d\rho(\rho') {}_0\kappa(\rho') (\mathcal{R}_\rho \Psi^j)^*(\rho'). \quad (\text{A1})$$

Additionally, the low frequency component of  ${}_0\kappa$  is encapsulated by the axisymmetric convolution with  $\Upsilon \in \ell^2_{\max}(S^2)$  such that,

$$s(\omega) = \int_{S^2} d\Omega(\omega') {}_0\kappa(\omega') (\mathcal{R}_\omega \Upsilon)^*(\omega'). \quad (\text{A2})$$

It is possible to project these directional and axisymmetric convolution operators into harmonic space (Wallis et al. 2017b),

$$(w^j)_{mn}^\ell \equiv \langle w^j, \mathcal{D}_{mn}^{\ell*} \rangle = \frac{8\pi^2}{2\ell+1} {}_0\kappa_{lm} \Psi_{\ell n}^{j*}, \quad (\text{A3})$$

$$s_{\ell m} \equiv \langle s, Y_{\ell m} \rangle = \sqrt{\frac{4\pi}{2\ell+1}} {}_0\kappa_{lm} \Upsilon_{\ell 0}^*. \quad (\text{A4})$$

The coefficients of a general spherical signal  ${}_s f$  can be synthesized exactly by

$${}_s f(\omega) = \int_{S^2} d\Omega s(\omega') (\mathcal{R}_{\omega'} s)(\omega') + \sum_{j=J_0}^J \int_{\text{SO}(3)} d\rho w^j(\rho') (\mathcal{R}_{\rho'} w^j)(\rho'), \quad (\text{A5})$$

from which we can define the discretized form of  ${}_0\kappa$  by

$${}_0\kappa(\omega) = \sum_{\ell=0}^{\infty} \sum_{m=-\ell}^{\ell} \left\{ \sqrt{\frac{4\pi}{2\ell+1}} s_{\ell m} \Upsilon_{\ell 0} Y_{\ell m}(\omega) + \frac{2\ell+1}{8\pi^2} \sum_{j=J_0}^{J_{\max}} \sum_{n=-\ell}^{\ell} (w^j)_{mn}^\ell \Psi_{\ell n}^j Y_{\ell m}(\omega) \right\}, \quad (\text{A6})$$

where the harmonic coefficients  ${}_0\kappa_{\ell m}$  are explicitly given by

$${}_0\kappa_{\ell m} = \sqrt{\frac{2\ell+1}{4\pi}} s_{\ell m} \Upsilon_{\ell 0} + \frac{2\ell+1}{8\pi^2} \sum_{j=J_0}^{J_{\max}} \sum_{n=-\ell}^{\ell} (w^j)_{mn}^\ell \Psi_{\ell n}^j. \quad (\text{A7})$$

Combining equations (A3) and (A4), the harmonic representation of the spherical wavelet transform at scale  $j$  can be written as a combination of the following linear operators (Wallis et al. 2017b):

$$\hat{w}^j = \mathbf{N}^j \mathbf{W}^j {}_0\hat{\kappa}_{\ell m},$$

are the Wigner coefficients of the directional wavelet coefficients. Here  $\mathbf{W}^j$  is harmonic space multiplication by the wavelet kernel  $\Psi_{\ell n}^{j*}$ , and  $\mathbf{N}^j$  corresponds to wavelet normalization.

$$\hat{s} = \mathbf{S} {}_0\hat{\kappa}_{\ell m},$$

are the spherical harmonic coefficients of the scaling wavelet coefficients, where  $\mathbf{S}$  is harmonic space multiplication by scaling kernel  $\Upsilon_{\ell 0}^*$ .

We further specialize by grouping the harmonic representation of the coefficients into  $\hat{\alpha} = \mathbf{N}\mathbf{W} {}_0\hat{\kappa}_{\ell m}$ , where the wavelet scale normalization terms are collectively  $\mathbf{N} = \text{diag}(\mathbb{1}, \mathbf{N}^{J_0}, \dots, \mathbf{N}^{J_{\max}})$ , and the Wigner/harmonic space wavelet convolutions are collectively  $\mathbf{W} = \text{diag}(\mathbf{S}, \mathbf{W}^{J_0}, \dots, \mathbf{W}^{J_{\max}})$ . Finally we introduce a diagonal array of operators  $\mathbf{H}$  corresponding to inverse spherical harmonic and Wigner transforms,  $\mathbf{H} = \text{diag}(\mathbf{Y}, \mathbf{D}^{J_0}, \dots, \mathbf{D}^{J_{\max}})$ . In the scope of this paper, we restrict ourselves to the analysis setting, thus these are the only operators required though a complete set are provided in Wallis et al. (2017b). Concatenating these operators we can finally form analysis forward and adjoint wavelet transforms,

$$\tilde{\Psi} = \mathbf{H}\mathbf{N}\mathbf{W}\tilde{\Upsilon} \quad \text{and} \quad \tilde{\Psi}^\dagger = \tilde{\Upsilon}^\dagger \mathbf{W}^\dagger \mathbf{N}\mathbf{H}^\dagger. \quad (\text{A8})$$

Note that  $\dagger$  is the adjoint (or conjugate transpose) operator, and as  $\mathbf{N}$  is simply wavelet scaling it is trivially self-adjoint  $\mathbf{N} = \mathbf{N}^\dagger$ . Crucially as we work in the discrete setting the inverse wavelet transforms are not equivalent to the adjoint wavelet transforms,<sup>13</sup> and so we adopt the optimized algorithms to compute fast Wigner and Wigner adjoint functions presented in the appendix of McEwen et al. (2015b).

<sup>13</sup>An approximation often made throughout the literature.

This paper has been typeset from a  $\text{\TeX}/\text{\LaTeX}$  file prepared by the author.